

## THE KECK + MAGELLAN SURVEY FOR LYMAN LIMIT ABSORPTION II: A CASE STUDY ON METALLICITY VARIATIONS

GABRIEL E. PROCHTER<sup>1</sup>, J. XAVIER PROCHASKA<sup>1</sup>, JOHN M. O'MEARA<sup>2,3</sup>, SCOTT BURLES<sup>3</sup>, REBECCA A. BERNSTEIN<sup>1</sup>

*Draft version June 11, 2018*

### ABSTRACT

We present an absorption line analysis of the Lyman limit system (LLS) at  $z \approx 3.55$  in our Magellan/MIKE spectrum of PKS2000–330. Our analysis of the Lyman limit and full H I Lyman series constrains the total H I column density of the LLS ( $N_{\text{HI}} = 10^{18.0 \pm 0.25} \text{ cm}^{-2}$  for  $b_{\text{HI}} \geq 20 \text{ km s}^{-1}$ ) and also the  $N_{\text{HI}}$  values of the velocity subsystems comprising the absorber. We measure ionic column densities for metal-line transitions associated with the subsystems and use these values to constrain the ionization state ( $> 90\%$  ionized) and relative abundances of the gas. We find an order of magnitude dispersion in the metallicities of the subsystems, marking the first detailed analysis of metallicity variations in an optically thick absorber. The results indicate that metals are not well mixed within the gas surrounding high  $z$  galaxies. Assuming a single-phase photoionization model, we also derive an  $N_{\text{H}}$ -weighted metallicity,  $\langle [\text{Si}/\text{H}] \rangle = -1.66 \pm 0.25$ , which matches the mean metallicity in the neutral ISM in high  $z$  damped Ly $\alpha$  systems (DLAs). Because the line density of LLSs is over  $10\times$  higher than the DLAs, we propose that the former dominate the metal mass-density at  $z \sim 3$  and that these metals reside in the galaxy/IGM interface. Considerations of a multi-phase model do not qualitatively change these conclusions. Finally, we comment on an anomalously large  $\text{O}^0/\text{Si}^+$  ratio in the LLS that suggests an ionizing radiation field dominated by soft UV sources (e.g. a starburst galaxy). Additional abundance analysis is performed on the super-LLS systems at  $z \approx 3.19$ .

*Subject headings:* large-scale structure of universe — quasars: absorption lines — intergalactic medium

### 1. INTRODUCTION

Lyman limit systems (LLSs) are the ‘clouds’ along quasar sightlines that have sufficient H I column density  $N_{\text{HI}}$  to be optically thick ( $\tau > 1$ ) at the Lyman limit, i.e.  $N_{\text{HI}} \gtrsim 10^{17.2} \text{ cm}^{-2}$ . This definition separates LLSs from the Ly $\alpha$  forest lines (clouds with typical  $N_{\text{HI}} < 10^{15} \text{ cm}^{-2}$ ) which trace the intergalactic medium (IGM; Rauch 1998) and the damped Ly $\alpha$  systems (DLAs;  $N_{\text{HI}} \geq 2 \times 10^{20} \text{ cm}^{-2}$ ) that trace high redshift protogalaxies (Wolfe et al. 2005). On the basis of their intermediate H I surface density, one may expect the LLSs to represent the physical interface between the IGM and high  $z$  galaxies. Studies of the LLSs, therefore, may constrain the accretion history of galaxies and the transport of material back to the IGM.

A key tracer of these processes is the metals intermixed with the gas. These are presumably formed in the deep potential wells of galaxies, imported to the interstellar medium by stellar winds and supernova explosions, and (possibly) carried to greater distances by tidal disruption and/or star-formation and AGN feedback processes. With the advent of the 10m Keck I telescope coupled with the HIRES echelle spectrometer (Vogt et al. 1994), observers demonstrated that a significant fraction of the IGM is enriched in heavy elements of C, Si, and O (Tytler et al. 1995; Cowie et al. 1995). More recent studies have established the variation of metallicity with density and redshift (Schaye et al. 2003; Simcoe et al. 2004; Aguirre et al. 2008) and demonstrate a me-

dian metallicity of roughly 1/1000 solar. These observations constrain the integrated enrichment by galaxies of their surrounding medium (e.g. Aguirre et al. 2001). Studies of the metallicity distribution and evolution in the damped Ly $\alpha$  systems (Pettini et al. 1994; Prochaska et al. 2003), meanwhile, constrain the star-formation history of high  $z$  galaxies and the processes of ISM enrichment (Dessauges-Zavadsky et al. 2004; Johansson & Efsthathiou 2006). These studies demonstrate that the ISM of most high  $z$  galaxies is metal-poor ( $\approx 1/30$  solar), that none have a metallicity less than 1/1000 solar, and that a wide dispersion ( $100\times$ ) exists from galaxy to galaxy (Prochaska et al. 2003).

Although precise measurements for over 100 damped Ly $\alpha$  galaxies have been acquired (Prochaska et al. 2003; Ledoux et al. 2006; Prochaska et al. 2007), constraints on metallicity variations within single galaxies are very limited. The metal-line transitions generally show absorption by multiple components spanning  $\approx 100 \text{ km s}^{-1}$  (Prochaska & Wolfe 1997), presumably by gas distributed on galactic (kpc) scales. The Lyman series, however, is in general too saturated to yield the H I column densities of the velocity components identified in the metal-line transitions. Therefore, these data provide little constraint on metallicity gradients along the sightline even as a function of velocity much less position. The studies to date have focused instead on relative abundance ratios within DLAs which best trace variations in the gas density, depletion, and/or ionization state (Prochaska & Wolfe 1996; Lopez et al. 2002; Prochaska 2003; Dessauges-Zavadsky et al. 2006).

In contrast to DLAs, the higher order Lyman series transitions of LLSs are often unsaturated and one may (in principal) resolve the H I absorption into multiple velocity components, each with a well-measured H I col-

<sup>1</sup> Department of Astronomy and Astrophysics, UCO/Lick Observatory, University of California, 1156 High Street, Santa Cruz, CA 95064

<sup>2</sup> Department of Chemistry and Physics, Saint Michael's College. One Winooski Park, Colchester, VT 05439

<sup>3</sup> Visiting Astronomer, Las Campanas Observatory

umn density. It would then be possible to explore variations in the physical conditions of these components, including the gas metallicity. This analysis has not been extensively pursued, primarily because of the significant observational demands: one requires high S/N, echelle observations covering the full Lyman series. This demands wavelength coverage  $\lambda < 4000\text{\AA}$  for sources at  $z < 3.4$  which is observationally challenging. The analysis, as well, is both time-consuming and limited by the uncertainties of photoionization modeling. With only a few exceptions (e.g. Prochaska & Burles 1999), the only LLSs analyzed thus far are the rare and special subset of LLS that are sufficiently quiescent kinematically to permit a measurement of the D/H ratio (Burles & Tytler 1998; Burles et al. 1999).

Researchers have focused instead on the integrated metallicities of the so-called super-LLS (SLLS; also referred to as sub-DLAs) with  $N_{\text{HI}} \geq 10^{19}\text{cm}^{-2}$  (Prochaska 1999; Péroux et al. 2003; Prochaska et al. 2006). The Ly $\alpha$  damping wings for these systems are resolved by high-resolution spectroscopy and therefore allow a precise constraint on their total  $N_{\text{HI}}$  value. In turn, the gas metallicity may be estimated subject to photoionization corrections. It is rare, however, that the full Lyman series is observed or analyzed, and absent the  $N_{\text{HI}}$  component structure one cannot study metallicity gradients.

This paper marks the second in a series presenting results on a survey of  $z \sim 3$  Lyman limit systems. In our first paper (O’Meara et al. 2007, ; hereafter Paper I), we presented constraints on the H I frequency distribution of the SLLSs absorbers with  $N_{\text{HI}} = 10^{19}\text{cm}^{-2}$  to  $10^{20.3}\text{cm}^{-2}$ , from a survey of echelle and echellette data. In this paper, we present our first detailed analysis of a Lyman limit system with  $N_{\text{HI}} \approx 10^{18}\text{cm}^{-2}$ . We demonstrate that one can precisely constrain the H I column densities of the metal-bearing ‘clouds’ in such systems when provided with high-resolution spectroscopy covering the full Lyman series. Furthermore, we measure the ionization state, metallicity, and relative abundances of the gas through comparisons with models of ionization equilibrium. In this fashion, we can also explore metallicity variation within the LLS, presumably corresponding to galactic (sub-Mpc) scales.

Our target is PKS2000–330, a bright ( $m_v = 17.3$ ) quasar at  $z_{em} = 3.77$  (Peterson et al. 1982) discovered by Jauncey et al. (1982). Several papers on the subject of absorption systems have targeted this quasar previously (Hunstead et al. 1986; Murdoch et al. 1986). These authors characterized the Ly $\alpha$  forest and the properties of several strong absorption systems along the sightline. In their spectra the authors describe four metal-line systems with H I absorption indicative of LLSs. Two are a close pair at  $z \approx 3.19$  characterized by typical low-ionization lines. Based on a measurement of the O I  $\lambda 1039$  line, the authors reported that one of these systems displays an enrichment level comparable to the Milky Way interstellar medium ( $\gtrsim \frac{1}{2}$  solar). The highest redshift system analyzed is the one responsible for the obvious LLS feature below  $\sim 4200\text{\AA}$ . At  $z_{abs} \sim 3.55$ , this was at the time the highest redshift LLS system studied. Limited by spectral resolution, the authors presented only a cursory analysis of its properties. These absorption systems,

especially the LLS, are the focus of the current paper<sup>4</sup>. Throughout the manuscript we assume the solar abundances reported by Grevesse et al. (2007).

## 2. DATA

We observed PKS2000–330 with the MIKE echelle spectrograph (Bernstein et al. 2003) on the Magellan II (Clay) Telescope for two 2,400 second exposures on the night of September 2, 2004. The MIKE spectrometer uses a dichroic centered at  $\lambda \approx 5000\text{\AA}$  to separate the optical light into two cameras where it is collimated and dispersed onto the SITE 2k x 4k  $15\mu\text{m}$  detectors. The data was reduced using the MIKE Reduction Pipeline<sup>5</sup> (Bernstein et al. 2008) which employs novel techniques for the flat fielding, sky subtraction, spectral extraction, wavelength and flux calibration of echelle spectroscopy. The reduction algorithms also estimate and subtract scattered light detected between the echelle orders. This signal smoothly varies across the image and has a negligible contribution compared to the sky, even at blue wavelengths.

The resolution of this data is FWHM  $\sim 10\text{ km s}^{-1}$  for the blue data (3200 – 5000  $\text{\AA}$ ) and  $\sim 12\text{ km s}^{-1}$  for the red data (5000 – 9000  $\text{\AA}$ ) as measured from a series of well-isolated arc lines. The signal-to-noise ( $S/N$ ) of the data is  $\approx 25$  per  $3\text{ km s}^{-1}$  and  $4.2\text{ km s}^{-1}$  pixel at  $\lambda = 4400\text{\AA}$  and  $6000\text{\AA}$ , on the blue and red sides respectively. Because of the differing spectral resolution, we did not coadd the blue and red-side data in the region of spectral overlap. Instead, we restrict the analysis of features at  $\lambda < 5000\text{\AA}$  to the blue-side spectrum and  $\lambda \geq 5000\text{\AA}$  to the red-side data.

The calibrated spectra are presented in Figure 1. It is our experience that the relative flux calibration is accurate to within 15% (Bernstein et al. 2008). To analyze the absorption lines in a quasar spectrum, one must first estimate its intrinsic continuum. We fit a series of b-splines and low-order polynomials to our spectrum of PKS2000–330 by interactively selecting regions where a visible inspection suggests minimal absorption, i.e. the regions were assumed to reflect the quasar continuum. This process is augmented with corrections made by hand, generally to maintain a smooth curve. The continuum estimate is the leading source of systematic error, especially for analysis within the Ly $\alpha$  forest. At this high redshift, there are few (if any) narrow bands of unabsorbed quasar light blueward of the Ly $\alpha$  emission peak. For spectra with S/N typical of our dataset, it is difficult to avoid a systematic underestimate of the continuum at these wavelengths. This is especially true for data blueward of the rest-frame Lyman limit for the quasar ( $\lambda < 4350\text{\AA}$ ) where absorption from all members of the Lyman series may contribute. In Figure 1 we show our estimate of the quasar continuum as a light dotted line. The reduced and normalized 1-d spectra are available at <http://www.uchicago.edu/~xavier/LLS>.

## 3. IONIC COLUMN DENSITIES

In this section, we discuss the techniques and measurement of ionic column densities for the gas comprising the

<sup>4</sup> The fourth system (at  $z = 3.33$ ) noted by Hunstead et al. (1986) has a poorly constrained  $N_{\text{HI}}$  value and we have chosen not to analyze its properties in detail.

<sup>5</sup> <http://web.mit.edu/~burles/www/MIKE/>

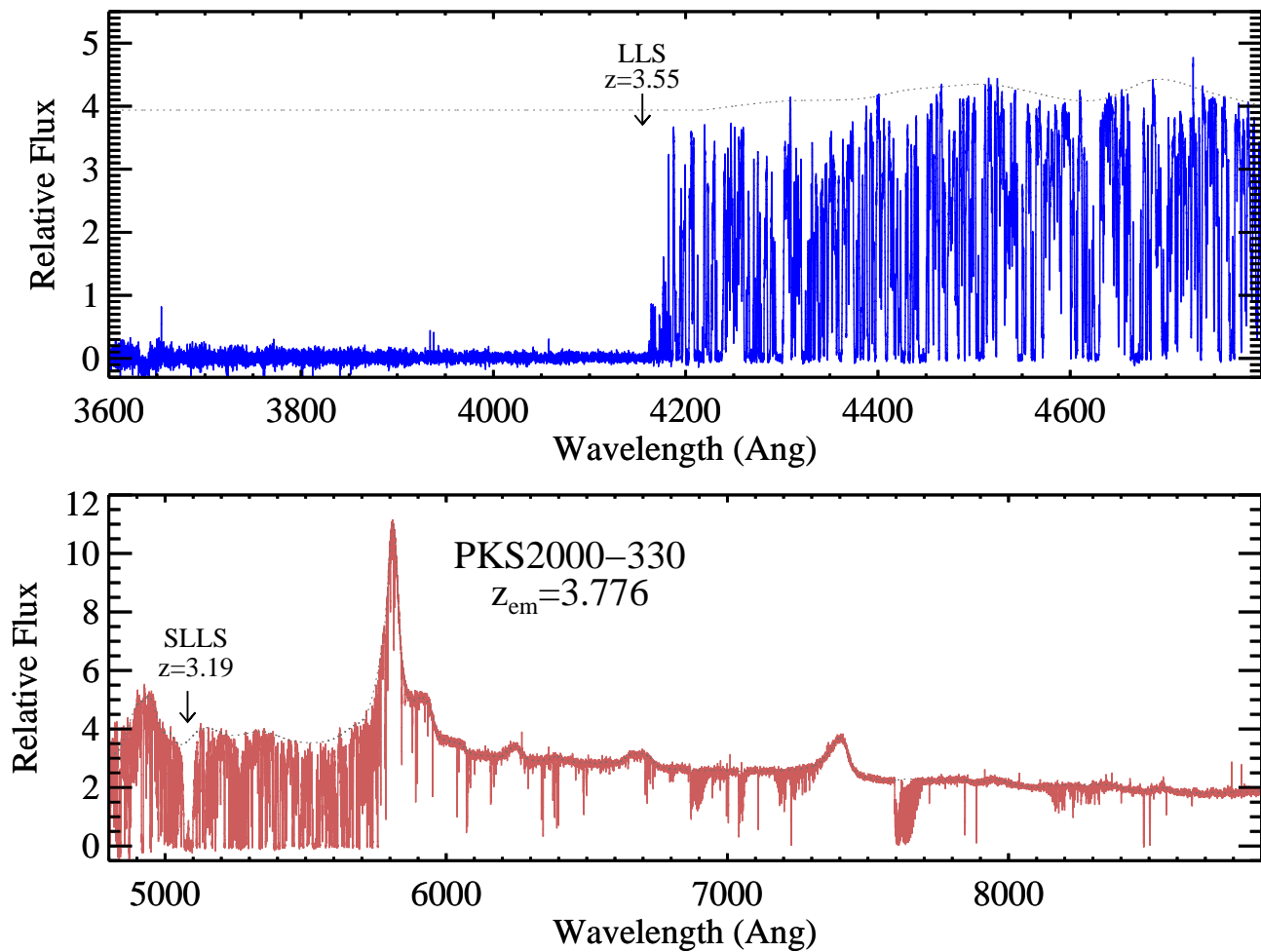


FIG. 1.— Magellan/MIKE spectrum of the quasar PKS2000–330 observed on the night of September 2, 2004 (4800s total exposure). The upper panel shows the data acquired through the red camera at a dispersion of  $\text{FWHM} \approx 12 \text{ km s}^{-1}$ . Strong  $\text{Ly}\alpha$  absorption from a complex of super-LLS is indicated at  $\lambda \approx 5100\text{\AA}$ . The lower panel plots the data acquired through the blue camera at a dispersion of  $\text{FWHM} \approx 10 \text{ km s}^{-1}$ . We mark the Lyman limit system at  $\lambda \approx 4100\text{\AA}$  corresponding to  $z \approx 3.55$ . The data have been smoothed in each panel by 3 pixels for presentation purposes only (finer detail cannot be resolved by this figure). The dotted line in each panel shows our estimate of the quasar continuum which is used to normalize the spectra for absorption-line analysis.

LLS at  $z \approx 3.55$  toward PKS2000–330. An analysis of the column densities for the SLLSs at  $z \approx 3.19$  is presented in Appendix B.

### 3.1. Techniques

The standard method of characterizing an absorption line is with a Voigt profile described by three physical parameters: the redshift  $z$ , the column density  $N$ , and the Doppler parameter ( $b \equiv \sigma\sqrt{2}$ ). These values bear upon the physical quantities that determine the gas ionization, most importantly the spatial density, kinematics, and temperature. To fit for these parameters, we employed the VPFIT software package kindly provided by R. Carswell and J. Webb<sup>6</sup>. For this software package, the user supplies (1) spectral regions for analysis, (2) a list of components with ions specified, (3) initial guesses for the parameter values, and (4) the spectral line-profile parameterized here as a Gaussian with FWHM estimated from the ThAr data. In our analysis, we have generally avoided spectral regions that are significantly blended with coincident  $\text{Ly}\alpha$  forest absorption

or coincident metal-line absorption. We typically have constrained the low-ion<sup>7</sup> components of a system to have identical redshift so that the redshift for each set of low-ion transitions of a given component are parameterized by a single value. This constraint is observationally motivated by the good alignment between the absorption lines in velocity space. For H I Lyman lines, which suffer from significant line-blending, we have anchored their redshift to the value derived from an independent fit of the metal-line transitions. This presumes that the H I absorption traces the low-ion profiles in velocity space, but the relative column densities are allowed to vary freely from component to component. Unfortunately, in the LLS presented here the line-blending is too severe to test the former assumption empirically. Future analysis of the other LLS in our survey will address this point although we note that such analysis is best performed in

<sup>7</sup> Low-ions are defined to be the first ionization state for a gas that has an ionization potential exceeding 1 Ryd (e.g.  $\text{O}^0$ ,  $\text{Si}^+$ ,  $\text{Fe}^+$ ). These atoms and ions are the dominant ionization state in a neutral hydrogen gas where a significant far-UV ( $h\nu \lesssim 13 \text{ eV}$ ) radiation field is present.

<sup>6</sup> See <http://www.ast.cam.ac.uk/~rfc/vpfit.html>

the low redshift universe where line-blending with the Ly $\alpha$  forest, is minimized (e.g. Lehner et al. 2009). For lines analyzed within the Ly $\alpha$  forest we allow for a systematic uncertainty in the continuum placement of 10%. This error does not dominate in any of the analysis presented in this paper. In general, our fits adopt the fewest components which yield reduced  $\chi^2$  values near unity.

We complement this line-profile analysis with ionic column densities measured from the apparent optical depth method (AODM; Savage & Sembach 1996). In the AODM, one converts the observed normalized flux profile ( $f$ ) to an apparent optical depth array  $\tau_a \equiv -\ln(1/f)$  and then sums over the velocity interval of the line-profile to calculate the integrated column density. This non-parametric technique provides accurate results for well-resolved profiles. It also provides conservative upper and lower limits for undetected or saturated lines. Throughout this paper, we adopt these limits where appropriate. Upper limits correspond to  $2\sigma$  statistical uncertainties and lower limits correspond to the column densities by demanding  $f \geq 1\sigma$  in every pixel. Finally, the AODM analysis is useful for identifying unresolved components (hidden saturation) by comparing the column densities of a series of transitions with different oscillator strengths from a single ion. This analysis is especially appropriate for our dataset because the spectral resolution is lower than the echelle data commonly used in quasar absorption line studies. For the atomic data, we have relied on the compilation of atomic data given by Morton (2003).

### 3.2. The $z \approx 3.55$ LLS Intervening PKS2000–330

The absorption system at  $z \approx 3.55$  gives rise to the strong Lyman limit observed in the spectrum of PKS2000–330 (Figure 1) and, therefore, is the only LLS showing the complete Lyman series. As demonstrated below, spectral coverage that includes the entire Lyman series is crucial to precisely constraining the H I column density. We place a lower limit on the total H I column density of this LLS by estimating an upper limit to the normalized flux shortward of the Lyman limit. In the spectral window  $\lambda = 4000 - 4050 \text{ \AA}$ , we measure an upper limit to the normalized flux  $f_{LL} < 0.004$  (95% c.l.) where we have conservatively allowed for a 50% lower continuum than presented in Figure 1. This implies a lower limit to the total H I column density of the LLS,  $N_{\text{HI}} > \tau_{LL}/\sigma(E) = 10^{17.7} \text{ cm}^{-2}$  where  $\tau_{LL} = \ln(1/f_{LL})$  and  $\sigma(E)$  is evaluated at  $E = 4025 \text{ \AA}/[911.76 \text{ \AA}(1+z_{LL})]$  Ryd. This assumes that the contribution of coincident absorption by the IGM and metal-lines is minor, which is reasonable for wavelengths longward of the next lower redshift LLSs. We have also ruled out coincident, strong Ly $\alpha$  absorption at these wavelengths by searching for corresponding metal-line absorption (e.g. C IV).

We can set a conservative upper limit on the total H I column density through analysis of the Ly $\alpha$  transition. Figure 2 presents the spectrum of covering the Ly $\alpha$  transition for the  $z \approx 3.55$  LLS. The dotted line at relative flux  $f \approx 3.44$  traces the continuum estimated from regions of minimal absorption within and nearby this spectral region. Overplotted on the data is the set of Ly $\alpha$  models corresponding to  $N_{\text{HI}} = 10^{18.1}$  to  $10^{18.85} \text{ cm}^{-2}$  for a single absorber centered at  $z = 3.5523$ , where the majority of H I gas is expected to lie (see below). The profile assuming  $N_{\text{HI}} = 10^{18.85} \text{ cm}^{-2}$  significantly underpredicts

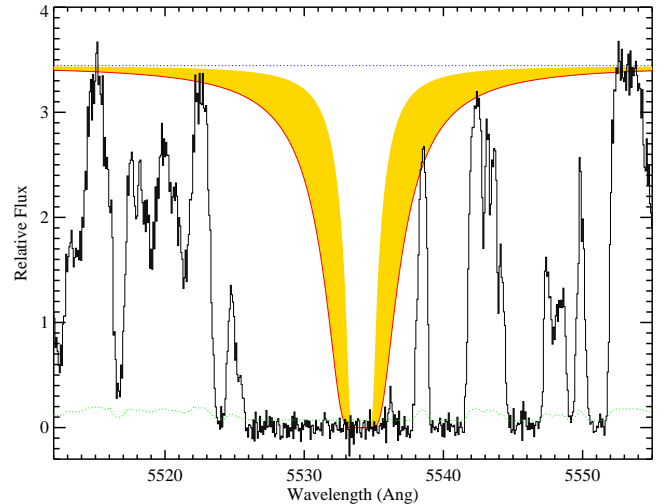


FIG. 2.— Spectral region encompassing the Ly $\alpha$  transition of the LLS at  $z \approx 3.55$ . The dotted line at relative flux  $f \approx 3.44$  traces the continuum estimated from assumed regions with minimal absorption within and nearby this spectral region. Overplotted on the data is the set of Ly $\alpha$  models corresponding to  $N_{\text{HI}} = 10^{18.1}$  to  $10^{18.85} \text{ cm}^{-2}$  (solid curve) for a single absorber centered at  $z = 3.5523$ , where the majority of H I gas is expected to lie in this LLS (see below). The profile assuming  $N_{\text{HI}} = 10^{18.85} \text{ cm}^{-2}$  significantly underpredicts the flux at  $\lambda \approx 5538.5 \text{ \AA}$ . Given that the flux at these wavelengths is further depressed by the ‘clouds’ centered at  $\lambda \approx 5537 \text{ \AA}$  and  $5540 \text{ \AA}$ , we adopt a conservative upper limit to the  $N_{\text{HI}}$  value at  $z = 3.5523$  of  $10^{18.85} \text{ cm}^{-2}$ .

the flux at  $\lambda \approx 5538.5 \text{ \AA}$ , especially if one accounts for the additional Ly $\alpha$  absorption from the clouds at  $\lambda \approx 5537 \text{ \AA}$  and  $5540 \text{ \AA}$ . We adopt a conservative upper limit for the gas at  $z = 3.5523$  of  $N_{\text{HI}} \leq 10^{18.85} \text{ cm}^{-2}$ .

A line-profile analysis of the full Lyman series will, in principle, give a more precise constraint on the H I column density of the LLS. Furthermore, such an analysis may also resolve the H I system into multiple velocity components. There are several challenges, however, to this analysis: (i) the various components of the LLS may blend with one another, especially in the higher-order Lyman series transitions; (ii) the Lyman series of the LLS is severely blended with the lower redshift IGM; and (iii) the majority of lines lie on the flat portion of the curve-of-growth implying a significant degeneracy between  $b$  and  $N_{\text{HI}}$ . We address the first concern (in part) by demanding that the strongest H I clouds have identical redshift as the strongest low-ion absorption. This requirement follows from the assumption that low-ions primarily arise in regions of large surface density of H I gas that can self-shield the material from ionizing photons. We address the second point by avoiding severely blended lines. On the third point, we consider physically plausible values for the Doppler parameter and adopt the corresponding  $N_{\text{HI}}$  constraints.

In Figure 3, we present a series of metal-line transitions for the LLS at  $z \approx 3.55$ . We have divided the line-profiles into three subsystems: (A)  $-230 \text{ km s}^{-1} \leq \delta v < -70 \text{ km s}^{-1}$ , (B)  $-70 \text{ km s}^{-1} \leq \delta v < 70 \text{ km s}^{-1}$ , and (C)  $70 \text{ km s}^{-1} \leq \delta v < 210 \text{ km s}^{-1}$  relative to  $z_{\text{LLS}} = 3.550$ . The velocity interval of the subsystems was chosen to separate the two significant low-ion complexes from each other (B and C) and also to separate strong C IV absorption (A) from the other subsystems. Subsystems B

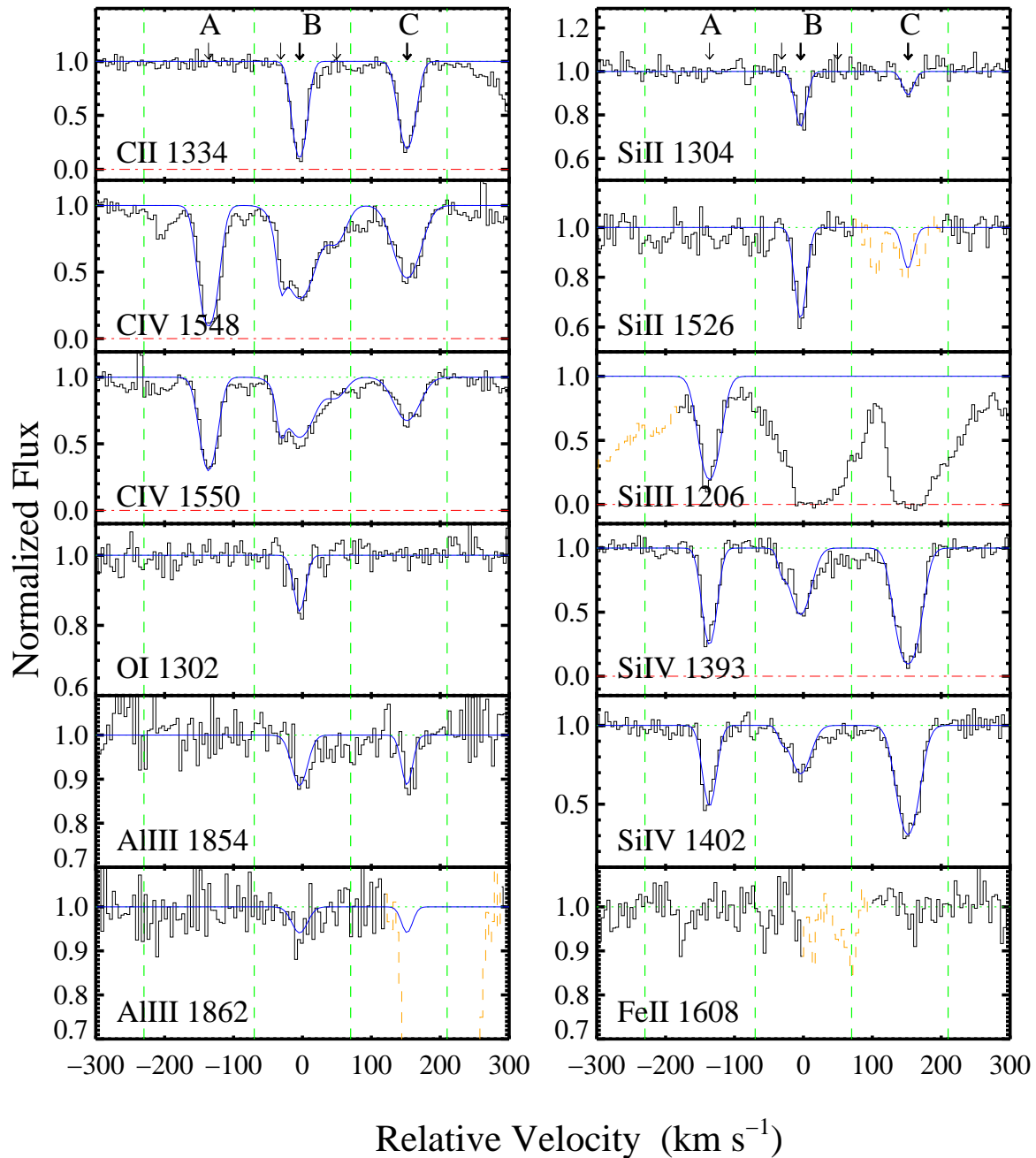


FIG. 3.— Velocity plot of the principal metal-line transitions detected for the LLS at  $z \approx 3.55$  ( $v = 0 \text{ km s}^{-1}$  corresponds to  $z = 3.550$ ). In each panel, the vertical (green) dashed lines designate three subsystems (A,B,C) that we have designated. Blends with coincident absorption (e.g. Ly $\alpha$  lines) are denoted as (orange) dashed spectra. Overplotted on the data is the best-fit solution from a line-profile analysis of the data using the VPFIT software package. Arrows in the top panels locate the centroids of the velocity components (Table 1).

and C show significant low-ion absorption and we expect that these contain the majority of the H I gas. We have independently fit the metal-line profiles of the various subsystems using the VPFIT software package. We have forced the components comprising each subsystem to have identical redshift for different low-ions but have allowed the Doppler parameter values to vary because the line widths of the high-ion transitions appear systematically wider than those of the low-ions. The best-fit solutions and  $1\sigma$  error estimates are presented in Table 1 and the models are overplotted on the data in Figure 3. The low and high-ion absorption in each subsystem is well

modeled by components having identical velocity, but the analysis also suggests that the high-ion gas has systematically larger Doppler parameters ( $b \gtrsim 20 \text{ km s}^{-1}$ ) than the low-ion gas ( $b \lesssim 15 \text{ km s}^{-1}$ ). This conclusion, however, is sensitive to the details of the component structure assumed in the analysis. It is possible to achieve an acceptable model where the  $b$ -values are identical between the low and high-ions, but this would require the inclusions of yet further components. The profile model presented here is the simplest one that reproduces the observations. We return to this point when discussing photoionization models of the system (§ 4). Finally, we

TABLE 1  
VPFIT SOLUTIONS FOR THE LLS AT  $z = 3.550$

Subsystem	$z$	$\sigma(z)$ ( $10^{-5}$ )	$v^a$ ( $\text{km s}^{-1}$ )	Ion	$b$ ( $\text{km s}^{-1}$ )	$\sigma(b)$ ( $\text{km s}^{-1}$ )	$\log N$	$\sigma(N)$
A	3.547932	0.5	-136	H I	17.45	3.27	14.88	0.10
				C IV	14.09	0.60	13.95	0.03
				Si IV	10.90	1.34	13.24	0.04
				Si III	16.68	1.32	13.00	0.03
B	3.549521	1.1	-32	C IV	3.00	1.56	13.23	0.16
				Si IV	3.00	9.69	12.09	0.17
B	3.549938	0.5	-4	H I	19.38	4.53	16.82	0.20
				C IV	27.48	1.53	13.89	0.03
				C II	10.01	0.64	14.09	0.04
				O I	9.24	3.78	13.34	0.09
				Al III	14.10	8.28	12.11	0.17
				Si II	8.97	1.50	13.27	0.04
				Si IV	17.97	1.53	13.11	0.03
				C IV	17.49	4.60	13.13	0.09
				C II	12.86	0.42	14.00	0.03
				Al III	8.58	0.42	11.96	0.18
C	3.550751	3.8	+50	H I	25.00	2.50	18.00	0.25
				C IV	23.71	1.11	13.65	0.03
C	3.552304	0.4	+152	C II	12.86	0.42	14.00	0.03
				Al III	8.58	0.42	11.96	0.18
				Si IV	18.67	0.48	13.64	0.03
				Si II	8.41	0.42	12.84	0.11

<sup>a</sup>Velocity relative to  $z = 3.550$ .

note that the regions containing the transitions of the O VI and N V doublets are hopelessly blended with co-incident IGM features.

The redshifts of the strongest low-ion component in each of the subsystems were then taken as an input constraint for the H I Lyman series analysis. In Figure 4, we present a subset of the Lyman series transitions and also a portion of the data near the Lyman limit. It is evident that the strongest, highly saturated members of the Lyman series offer only a weak constraint on the H I column densities of the subsystems. We first visually identified spectral regions that were most likely to constrain the strongest H I components of subsystems A, B, and C. We then inputted to VPFIT these regions, a set of H I absorption lines at the redshifts of each subsystem ( $z_A = 3.547932$ ,  $z_B = 3.549938$ ,  $z_C = 3.552304$ ), and additional H I lines within subsystem B (with  $z_C > z > z_B$ ) to model additional absorption evident in the Lyman series. The non-zero flux at  $\delta v \approx 50 \text{ km s}^{-1}$  in the high-order Lyman series lines (e.g. H I 918, 919) indicates that the integrated column densities of these additional components is significantly lower than the H I column density of subsystem C and possibly subsystem B. We can set a conservative upper limit to the total  $N_{\text{HI}}$  of this gas by integrating the apparent optical depth of the H I 918 profile in the interval  $\delta v = +17$  to  $+80 \text{ km s}^{-1}$ , finding  $N_{\text{HI}} < 10^{16.9} \text{ cm}^{-2}$  (95% c.l.). This value is to be considered an upper limit because there may be significant line-blending with lines from lower redshift IGM systems.

Our trials with the VPFIT package yielded a set of models with acceptable reduced  $\chi^2$  values, but we found that the parameters of the additional components in subsystem B are very poorly constrained and that we could not achieve a unique solution for the full set of profiles. Therefore, we used the range of solutions to guide a ‘by-eye’ fitting analysis of the components at  $z = z_B$  and  $z_C$ . The parameters for the gas at  $z = z_B$  are well constrained by the higher order Lyman series (H I 918,919,920,923):

$\log N_{\text{HI}} = 16.8 \pm 0.2$ ,  $b_{\text{HI}}^B = 19.4 \pm 4.5 \text{ km s}^{-1}$ . There is a weak dependence of these values on our assumed parameters for absorption at  $\delta v \approx +20 \text{ km s}^{-1}$  which contributes to our error estimate. Nevertheless, the total  $N_{\text{HI}}$  value for the gas in subsystem B is much less than that required to explain the observed absorption at  $\lambda < 4150 \text{ \AA}$ . We conclude that the majority of H I gas in the LLS at  $z \approx 3.55$  is associated with subsystem C.

The detection of positive flux at  $\delta v \approx +180 \text{ km s}^{-1}$  in H I 937 and at  $\delta v \approx +80 \text{ km s}^{-1}$  in H I 918,919 sets an upper limit to the combined  $N_{\text{HI}}$  and  $b_{\text{HI}}^C$  values of an H I component centered at  $z = z_C$ . Formally, the data permit  $N_{\text{HI}}$  values as large as  $10^{18.85} \text{ cm}^{-2}$  provided  $b$ -values less than  $10 \text{ km s}^{-1}$ . We adopt a prior of  $b_{\text{HI}}^C \geq 20 \text{ km s}^{-1}$ , however, based on the following physical arguments. First, we demonstrate in the following section that the gas related to subsystem C is highly ionized. Even if we assume a soft (i.e. stellar) ionizing radiation field, the implied gas temperature is  $T > 15,000 \text{ K}$  giving  $b > 16 \text{ km s}^{-1}$ . Second, systems with  $b \leq 20 \text{ km s}^{-1}$  are extremely rare, as evidenced by the rarity of D/H measurements from the IGM. Third, the C II transitions have Doppler parameters  $b > 10 \text{ km s}^{-1}$  which set a lower limit to the Doppler parameter of the H I gas. Finally, a model with  $b \leq 20 \text{ km s}^{-1}$  would underpredict the absorption at  $\delta v \approx -45 \text{ km s}^{-1}$  and  $+60 \text{ km s}^{-1}$  for the entire Lyman series. Therefore, one would need to introduce an additional 10 or more absorption lines (including many at unrelated redshifts) to reproduce the observations. Together, these points motivate a lower limit to  $b_{\text{HI}}^C$  of  $\approx 20 \text{ km s}^{-1}$ .

With this prior on  $b_{\text{HI}}^C$ , the data require  $N_{\text{HI}} < 18.5 \text{ cm}^{-2}$  and we adopt a best-estimate of  $N_{\text{HI}} = 10^{18.0 \pm 0.25} \text{ cm}^{-2}$  and  $b_{\text{HI}}^C = 25 \pm 2.5 \text{ km s}^{-1}$  for subsystem C. We caution that subsequent analysis should not treat the  $N_{\text{HI}}$  or  $b$ -values for subsystem C as following a normal distribution with the reported uncertainties. Instead, we recommend that the central value be considered uniformly distributed. But we also note that the



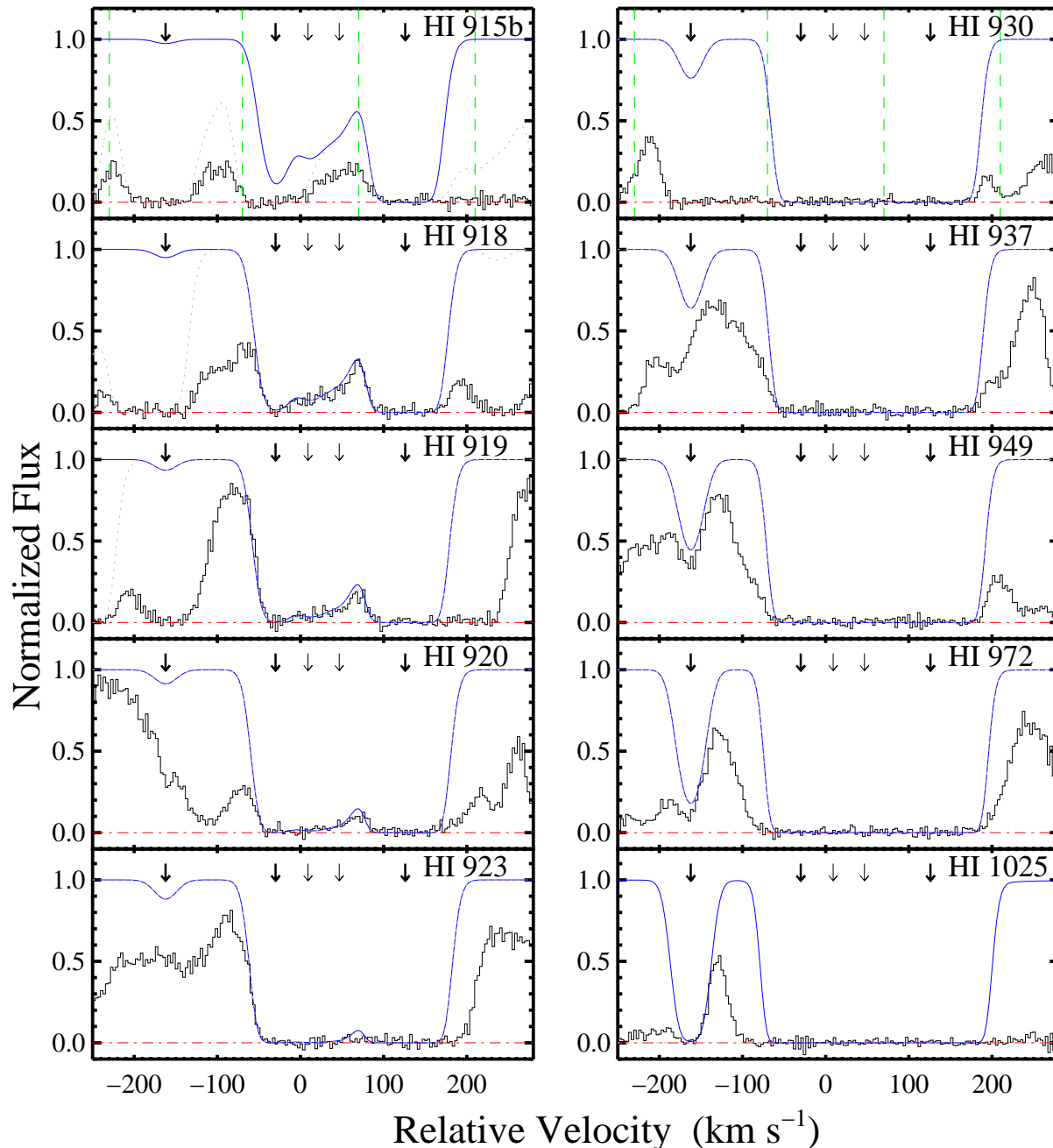


FIG. 4.— Velocity plots of the Lyman limit (upper-left panel) and a set of H I Lyman series transitions for the LLS at  $z \approx 3.55$  toward PKS2000–330. Arrows designate the centroids of the various velocity components used in the analysis (Table 1). The solid blue curve shows the convolved line-profile for each Lyman line individually, while the dotted gray curve plots the convolved solution for all Lyman lines (inspect the panel showing the H I 918 transition where multiple Lyman lines overlap). The vertical dashed lines in the panels showing H I 915b and 930 designate subsystems A, B, and C. The velocity  $v = 0 \text{ km s}^{-1}$  corresponds to an arbitrary  $z = 3.550$ .

$N_{\text{HI}}$  value cannot be significantly less than  $10^{17.7} \text{ cm}^{-2}$  because of the combined constraints from the Lyman limit and subsystem B.

The full set of constraints on the  $N_{\text{HI}}$  values for the subsystems comprising this LLS is summarized in Table 2. Our favored solution is overplotted on the data in Figure 4. It is evident that the strongest members of the Lyman series ( $\alpha, \beta, \gamma, \delta$ ) offer little constraint on the  $N_{\text{HI}}$  values of subsystems B and C. The best constraints come from higher order lines; these are presented in Figure 5. In this figure, we present the favored solution (middle panel) and  $2\sigma$  departures in the  $N_{\text{HI}}$  and  $b$  val-

TABLE 2  
CONSTRAINTS ON  $N_{\text{HI}}$  FOR THE LLS AT  $z = 3.550$

Subsystem	Feature	$\log N_{\text{HI}}$	Assumptions
A+B+C	Lyman Limit	$> 17.7$	Minimal IGM blending
C	Ly $\alpha$	$< 18.85$	None
A	Ly $\beta, \text{Ly}\gamma, \text{Ly}\delta$	$15.0 \pm 0.1$	Minimal IGM blending
B	Ly8-11	$16.8 \pm 0.2$	Minimal IGM blending
C	Ly5, Ly10-11	$18.0 \pm 0.25$	$b \geq 20 \text{ km s}^{-1}$

ues (incremented in opposition to minimize the change to

TABLE 3  
IONIC COLUMN DENSITIES FOR THE LLS AT  $z = 3.55$

Ion	$\lambda_{\text{rest}}$ (Å)	$\log f$	$v_{\text{int}}^a$ ( $\text{km s}^{-1}$ )	$\log N_{\text{AODM}}$	$\log N_{\text{VPFIT}}$	$\log N_{\text{adopt}}$
SUBSYSTEM A						
H I	1215.6701	-0.3805				$14.88 \pm 0.20$
C II	1334.5323	-0.8935	[-186, -86]	< 12.75		< 12.75
C IV	1548.1950	-0.7194	[-186, -96]	$13.91 \pm 0.03$	$13.95 \pm 0.03$	$13.95 \pm 0.03$
	1550.7700	-1.0213	[-186, -96]	$13.93 \pm 0.03$		
O I	1302.1685	-1.3110	[-166, -96]	< 13.00		< 13.00
Al III	1854.7164	-0.2684	[-186, -86]	< 12.12		< 12.12
	1862.7895	-0.5719	[-186, -86]	< 12.37		
Si II	1304.3702	-1.0269	[-186, -86]	< 12.80		< 12.72
	1526.7066	-0.8962	[-166, -96]	< 12.72		
Si III					$13.00 \pm 0.03$	$13.00 \pm 0.03$
Si IV	1393.7550	-0.2774	[-186, -96]	$13.14 \pm 0.03$	$13.24 \pm 0.04$	$13.24 \pm 0.04$
	1402.7700	-0.5817	[-186, -96]	$13.23 \pm 0.03$		
Fe II	1608.4511	-1.2366	[-186, -86]	< 12.93		< 12.93
SUBSYSTEM B						
H I	1215.6701	-0.3805				$16.82 \pm 0.20$
C II	1036.3367	-0.9097	[-47, 33]	$14.12 \pm 0.03$	$14.09 \pm 0.04$	$14.09 \pm 0.04$
	1334.5323	-0.8935	[-57, 43]	$14.03 \pm 0.03$		
	1335.7077	-0.9397	[-47, 23]	< 13.36		
C IV	1548.1950	-0.7194	[-57, 33]	$13.89 \pm 0.03$	$14.03 \pm 0.03$	$14.03 \pm 0.03$
	1550.7700	-1.0213	[-57, 33]	$14.05 \pm 0.03$		
O I	1302.1685	-1.3110	[-37, 33]	$13.35 \pm 0.07$	$13.34 \pm 0.09$	$13.34 \pm 0.09$
Al III	1854.7164	-0.2684	[-57, 43]	$12.19 \pm 0.13$	$12.11 \pm 0.17$	$12.11 \pm 0.17$
	1862.7895	-0.5719	[-57, 43]	< 12.38		
Si II	1304.3702	-1.0269	[-57, 43]	$13.21 \pm 0.06$	$13.27 \pm 0.04$	$13.27 \pm 0.04$
	1526.7066	-0.8962	[-37, 33]	$13.29 \pm 0.03$		
Si IV	1393.7550	-0.2774	[-57, 33]	$13.14 \pm 0.03$	$13.15 \pm 0.03$	$13.15 \pm 0.03$
	1402.7700	-0.5817	[-57, 33]	$13.18 \pm 0.03$		
Fe II	1608.4511	-1.2366	[-57, 43]	< 13.09		< 13.09
SUBSYSTEM C						
H I	1215.6701	-0.3805				$18.00 \pm 0.25$
C II	1036.3367	-0.9097	[112, 192]	$14.20 \pm 0.03$	$14.00 \pm 0.03$	$14.00 \pm 0.03$
	1334.5323	-0.8935	[102, 202]	$13.97 \pm 0.03$		
	1335.7077	-0.9397	[122, 192]	$12.90 \pm 0.10$		
C IV	1548.1950	-0.7194	[102, 192]	$13.65 \pm 0.03$	$13.65 \pm 0.03$	$13.65 \pm 0.03$
	1550.7700	-1.0213	[102, 192]	$13.64 \pm 0.03$		
O I	1302.1685	-1.3110	[122, 192]	< 13.01		< 13.01
Al III	1854.7164	-0.2684	[102, 202]	< 12.13	$11.96 \pm 0.18$	$11.96 \pm 0.18$
	1862.7895	-0.5719	[102, 202]	< 14.04		
Si II	1304.3702	-1.0269	[112, 192]	$12.79 \pm 0.14$	$12.84 \pm 0.11$	$12.84 \pm 0.11$
Si III	1206.5000	0.2201	[102, 202]	> 13.59		> 13.59
Si IV	1393.7550	-0.2774	[102, 192]	$13.60 \pm 0.03$	$13.64 \pm 0.03$	$13.64 \pm 0.03$
	1402.7700	-0.5817	[102, 192]	$13.62 \pm 0.03$		
Fe II	1608.4511	-1.2366	[102, 202]	< 12.91		< 12.91

<sup>a</sup>Velocity interval for the AODM relative to  $z = 3.550000$ .

the model). The shaded regions identify the pixels that most constrain these parameters. A few points should be emphasized. First, the left-hand panels correspond to a model with  $N_{\text{HI}} = 10^{17.5} \text{ cm}^{-2}$  which is ruled out by observations of the Lyman limit (see above). Second, the model in the right-hand panel significantly underpredicts the absorption at  $\delta v \approx +65 \text{ km s}^{-1}$ . Full coverage of the Lyman series and the Lyman continuum region at a relatively high S/N ratio has constrained the  $N_{\text{HI}}$  value of this LLS. Such analysis demands echelle spectra of the full Lyman series can minimize blending with the  $z \sim 3$  IGM and the foreground LLSs. The full set of ionic column densities for the three subsystems is provided in Table 3.

Before concluding our discussion on the H I absorption of the LLS at  $z \approx 3.55$ , we remark that our model

is not a good fit to the spectrum at  $\lambda \approx 4160 - 4175 \text{ \AA}$ . In this spectral range, which corresponds to the Ly-12, Ly-13, and Ly-14 transitions of the LLS, our model underpredicts the absorption at velocities in between the main components (i.e. away from the line centers). This implies either an additional source of nearly continuous opacity unrelated to the LLS at  $z = 3.55$  or that we have significantly overestimated the quasar continuum flux at these wavelengths. Comparing to the published spectrum of Barthel et al. (1990), we note a similar drop in the quasar flux at these wavelengths which argues against the latter explanation. Our expectation, therefore, is that the majority of additional opacity is from unidentified H I lines from the intergalactic medium at  $z < 3.55$ . In any case, the measurements of  $N_{\text{HI}}$  for this LLS are well constrained by the Lyman lines redward of  $4180 \text{ \AA}$ .



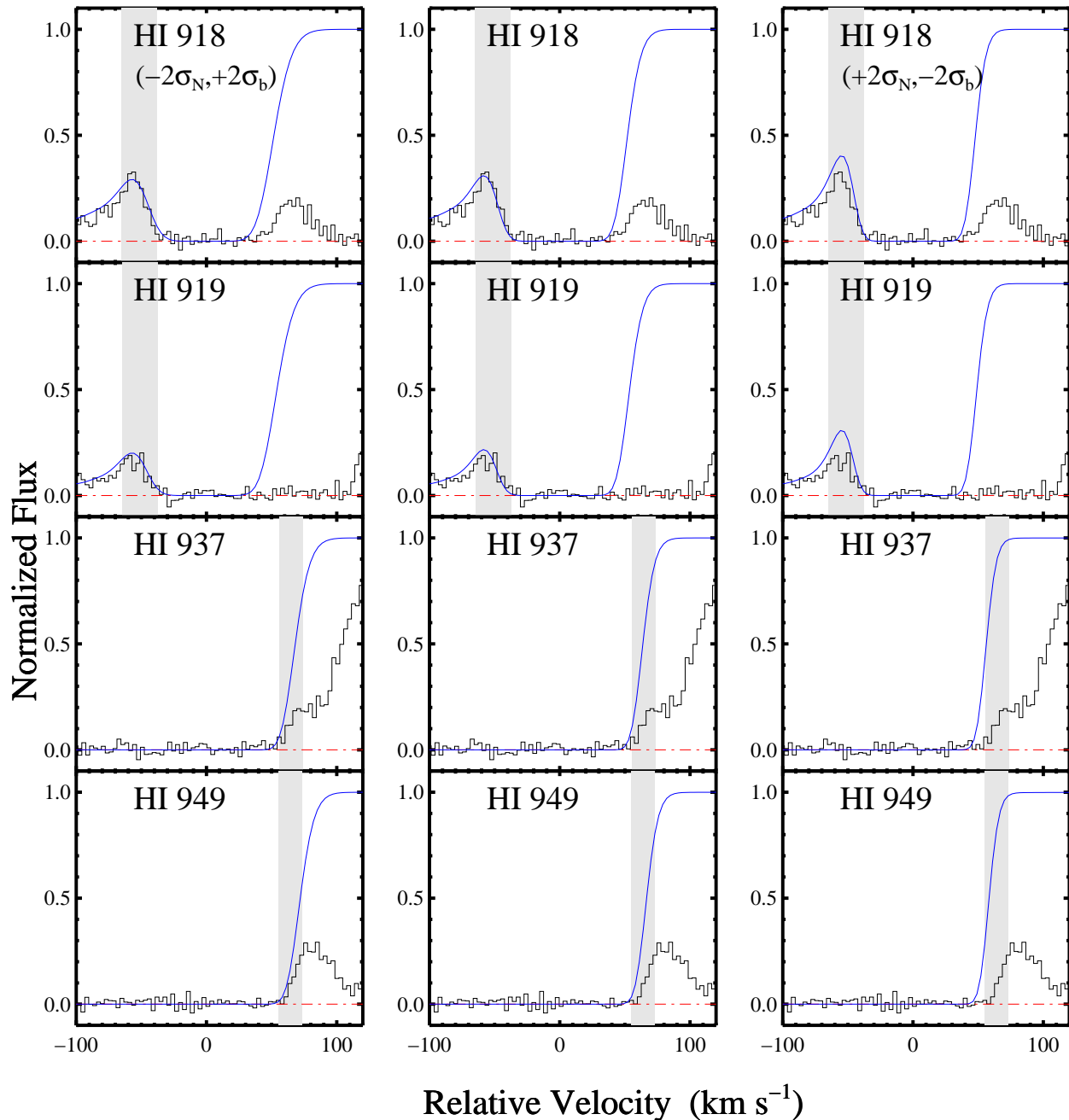


FIG. 5.— Zoom-in on the Lyman series lines that most tightly constrain the column densities and  $b$ -values for the H I components comprising subsystem C. The center panels show the favored model (solid blue curve) line for the central values of our line-profile solution while the left/right panels show  $2\sigma$  departures from the central value chosen to minimize changes in the model, i.e. an increase in  $N_{\text{HI}}$  is offset by a decrease in the  $b$ -value. The shaded boxes show the portion of the data that has greatest constraint on the analysis.

#### 4. PHOTOIONIZATION MODELING

At  $z > 2$ , gas clouds with H I column densities of less than  $10^{19} \text{ cm}^{-2}$  are predicted to be photoionized by the extragalactic ultra-violet background (EUVB) radiation field unless one assumes an extraordinarily high volume density (e.g. Viegas 1995). In this photoionized gas, the ions observed (especially the low-ions and H I) may represent only a trace quantity of the total gas present. To determine the gas abundance and also assess the physical conditions, it is necessary to model the ionization state of the gas. We have performed this modeling for the LLSs along the sightline to PKS2000–330 using the Cloudy software package (Ferland et al. 1998). In practice, we

have calculated ionization models for a series of plane-parallel slabs with constant gas density  $n_H$  and with  $N_{\text{HI}}$  constrained to match the central values derived from our line-profile analyses. We have adopted the EUVB radiation field calculated by Haardt & Madau (in prep.; a.k.a. CUBA) assuming contributions from both quasars and UV-bright galaxies. We run models with a wide range of ionization parameters  $U \equiv \Phi/n_{\text{HC}}$ , which is akin to adopting an intensity  $\Phi$  for the EUVB<sup>8</sup> and varying the Hydrogen volume density  $n_H$ . Finally, we compare ob-

<sup>8</sup> This intensity has been poorly constrained by empirical observation, but see Dall’Aglio et al. (2008).

served ionic ratios against the model predictions to constrain the ionization parameter  $U$  under the assumptions of our simplistic photoionization model. Ideally, we consider only pairs of ions from the same element to minimize dependence on the assumed intrinsic abundances. But we also find valuable constraints from ions of different elements, even allowing for significant departures from non-solar relative abundances. We caution that the single-phase models considered here are overly simplistic. In Appendix A, we present two-phase models to explore the impact of more complex scenarios.

As noted above, an absorption system with  $N_{\text{HI}} \ll 10^{20} \text{ cm}^{-2}$  is predicted to be highly ionized at  $z > 3$  by the EUVB radiation field alone. One signature of significant photoionization is the presence of strong high-ion absorption (C IV, Si IV) relative to low-ion species. Indeed, we find that the ratios of  $\text{C}^+/\text{C}^{3+}$  and  $\text{Si}^+/\text{Si}^{3+}$  are of order unity for subsystems B and C and much less than one for subsystem A. Under the assumption of a single-phase model, these observations indicate the gas in this LLS is predominantly ionized. As noted in § 3.2, however, the high-ion gas may have systematically larger Doppler parameters than the low-ion species. This might indicate that the gas occurs in a distinct region, physically separated by a large distance from the low-ion gas. We consider this hypothesis improbable because (i) it would require a remarkable coincidence for the low-ions and high-ions to arise in truly distinct ‘clouds’ yet share the same velocity; and (ii) the low  $N_{\text{HI}}$  of this LLS requires high ionization fractions and corresponding Si IV, C IV absorption unless one invokes a very large gas density  $n_H \gtrsim 0.1 \text{ cm}^{-3}$  (see Appendix A). We attribute the differences in  $b$ -values to the effects of photoionization from external sources onto an optically thick, self-shielding gas. Optical depth effects imply that the lower ionization states lie preferentially toward the middle of the absorbing gas while the high-ion gas arises in the outer regions. In this scenario, one expects a temperature gradient which would imply higher  $b$ -values for the high-ions. One can also allow for (and may even expect) a gradient in velocity dispersion that would further boost the Doppler parameters. A full treatment of such a model is beyond the scope of this paper. We proceed assuming a single-phase (constant density), optically thick model and restrict the ionic ratios to the gas at the velocities  $\delta v = -162, -30, +126 \text{ km s}^{-1}$  as listed in Table 1. In Appendix A, we explore how the results vary if we assume that the majority of the high-ion absorption is unrelated to the low-ion gas. We find that the principal scientific conclusions are qualitatively the same.

In Figure 6 we present the predicted ratios for pairs of ions observed in the LLS. Overplotted on the curves are the observed values (assuming a minimum uncertainty of 0.15 dex) where the horizontal error bars indicate the implied constraints for the ionization parameter. Allowing for the significant uncertainties inherent to this modeling (simplistic geometry, uncertain atomic data, etc.), the observations are broadly consistent with taking  $\log U_A = -1.8 \pm 0.3$ ,  $\log U_B = -2.8 \pm 0.2$ , and  $\log U_C = -2.4 \pm 0.2$  for the three subsystems. These values are typical of the ionization parameters derived for a handful other LLSs to date (e.g. Burles & Tytler 1998; Prochaska 1999; Prochaska & Burles 1999; Prochaska & Hennawi 2009). These estimated  $1\sigma$  uncertainties are

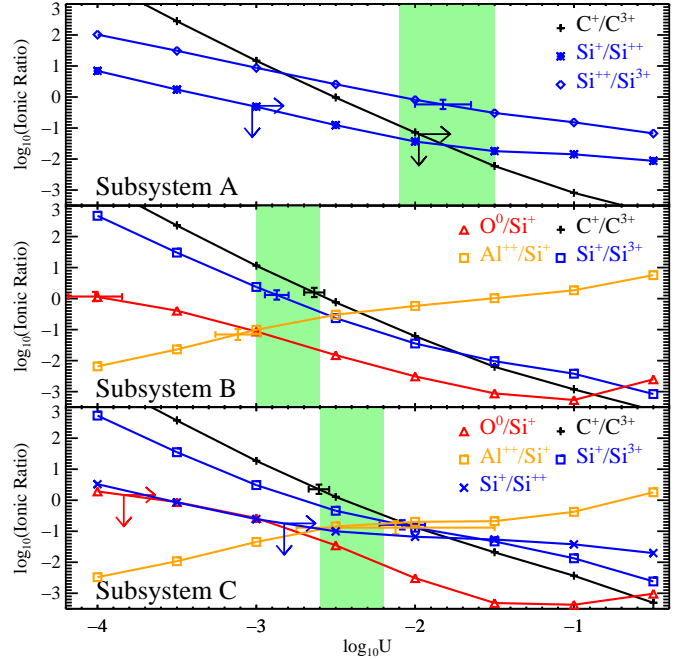


FIG. 6.— These curves show the predictions from a series of Cloudy photoionization models for the column density ratios of Si, C and O atoms and ions. The models are parameterized by the ionization parameter  $U$  which corresponds to the ratio of ionizing photons to hydrogen atoms per unit volume. In each panel, we have tuned the Cloudy models to match the observed  $N_{\text{HI}}$  values and metallicities of subsystems A, B, and C from the LLS at  $z \approx 3.55$ . Overplotted on the curves are the observational constraints. We have used these to estimate the ionization parameter for each subsystem (designated by the shaded regions in each panel).

dominated by systematic (not statistical) uncertainty. Note that the results do not change even if we assume that 90% of the high-ions arise in an alternate phase (Appendix A). This is because the curves involving Si IV and C IV are steep functions of  $\log U$ . We also note that the  $\text{Al}^+/\text{Si}^+$  observations indicate a significantly ionized gas even for our assumed solar intrinsic Al/Si abundance.

All of the observed ionic ratios are roughly consistent with the assumed  $U$  values save one: the  $\text{O}^0/\text{Si}^+$  ratio for subsystem B. In this subsystem, the observed column density ratio is  $\log[N(\text{O}^0)/N(\text{Si}^+)] = +0.03 \pm 0.1$  yet the photoionization model predicts  $N(\text{O}^0) \ll N(\text{Si}^+)$  for solar relative abundances and  $\log U_B > -4$ . At our preferred value of  $\log U_B = -2.80$ , the disparity between model and observation exceeds *one order of magnitude*. We have carefully considered the possibility that the absorption line at  $\lambda = 5925 \text{ \AA}$  identified as O I 1302 is a mis-identification, especially in light of its non-detection in subsystem C. The line, however, is not associated with the other subsystems, the SLLSs at  $z \sim 3.19$ , the Mg II absorber at  $z \approx 2.03$ , C IV 1548, nor any other frequently observed doublet of the IGM. We are confident in the identification, therefore, but are challenged to explain the offset between observation and model in the  $\text{O}^0/\text{Si}^+$  ratio. One possibility is that the gas has a highly super-solar O/Si ratio, i.e.,  $[\text{O}/\text{Si}] \gg 0$ . This runs contrary, however, to theoretical expectation (and empirical observations) that  $\alpha$ -elements roughly trace one another because they are both produced mainly by massive stars. At most, one might allow for departures from the solar abundances of  $\approx 0.3$  dex.

TABLE 4  
ELEMENTAL ABUNDANCES  
FOR THE LLS AT  $z \approx 3.55$

Ion	[X/H]	[X/Si <sup>+</sup> ]
Subsystem A <sup>a</sup>		
C <sup>+</sup>	< +0.08	< -0.91
C <sup>+3</sup>	-0.33 ± 0.50	-1.32 ± 0.63
O <sup>0</sup>	< +4.00	< +3.01
Al <sup>++</sup>	< +0.53	< -0.47
Si <sup>+</sup>	< +0.99	
Si <sup>+3</sup>	-0.16 ± 0.24	-1.15 ± 0.37
Fe <sup>+</sup>	< +3.86	< +2.87
Subsystem B <sup>b</sup>		
C <sup>+</sup>	-0.66 ± 0.20	-0.05 ± 0.20
C <sup>+3</sup>	-0.10 ± 0.48	+0.50 ± 0.49
O <sup>0</sup>	> -0.14	> -1.08
Al <sup>++</sup>	-0.95 ± 0.20	-0.35 ± 0.20
Si <sup>+</sup>	-0.61 ± 0.20	
Si <sup>+3</sup>	-0.73 ± 0.40	-0.13 ± 0.40
Fe <sup>+</sup>	< +0.45	< +1.05
Subsystem C <sup>c</sup>		
C <sup>+</sup>	-1.89 ± 0.20	+0.30 ± 0.20
C <sup>+3</sup>	-2.34 ± 0.43	-0.14 ± 0.35
O <sup>0</sup>	< -0.36	< +1.83
Al <sup>++</sup>	-2.26 ± 0.20	-0.07 ± 0.20
Si <sup>+</sup>	-2.19 ± 0.20	
Si <sup>+3</sup>	-1.85 ± 0.33	+0.34 ± 0.25
Fe <sup>+</sup>	< -0.65	< +1.54

NOTE. — In all cases, we have assumed a minimum error of 0.2 dex due to systematic errors in the photoionization modeling.

<sup>a</sup>Assumes a Cloudy photoionization model with  $N_{\text{HI}} = 10^{16.7} \text{ cm}^{-2}$ ,  $[\text{M}/\text{H}] = -0.50$  and  $\log U = -1.8 \pm 0.3$  dex

<sup>b</sup>Assumes a Cloudy photoionization model with  $N_{\text{HI}} = 10^{16.9} \text{ cm}^{-2}$ ,  $[\text{M}/\text{H}] = -0.50$  and  $\log U = -2.8 \pm 0.2$  dex

<sup>c</sup>Assumes a Cloudy photoionization model with  $N_{\text{HI}} = 10^{17.9} \text{ cm}^{-2}$ ,  $[\text{M}/\text{H}] = -1.50$  and  $\log U = -2.4 \pm 0.2$  dex

The predicted low value for the O<sup>0</sup>/Si<sup>+</sup> ratio from our models with  $\log U > -4$  stem primarily from the large cross-section of O<sup>0</sup> to extreme ultraviolet and x-ray photons (Sofia & Jenkins 1998). If one adopts a softer spectrum (i.e. one absent the influence of quasars), the O<sup>0</sup>/Si<sup>+</sup> ratio tends toward the intrinsic O/Si abundance, e.g.  $\log[N(\text{O}^0)/N(\text{Si}^+)] \approx +1$  for solar relative abundances. It is possible that the observed ratio,  $\log[N(\text{O}^0)/N(\text{Si}^+)] \approx 0$ , indicates a softer radiation field than we have adopted. This would require an intense and local source of radiation, e.g. the UV flux from a star-burst galaxy. Deep imaging of the field does not reveal any nearby bright source of UV flux (O’Meara et al. 2006). We proceed by adopting the ‘quasar+galaxy’ EUVB model and report the O/H abundance as a lower limit from the observed O<sup>0</sup>/H<sup>0</sup> ratio. Interestingly, this yields  $[\text{O}/\text{H}] > -0.1$  dex, a limit that lies three times above the ionization corrected  $[\text{Si}/\text{H}]$  value. We note that a softer ionizing spectrum would also imply a higher Si/H

TABLE 5  
SUMMARY OF PROPERTIES FOR THE LLS AT  $z \approx 3.55$

Property	A	B	C
$\log(N_{\text{HI}}/\text{cm}^{-2})$	14.9 ± 0.20	16.82 ± 0.20	18.0 ± 0.25
$\log U$	-1.8 ± 0.3	-2.8 ± 0.2	-2.4 ± 0.2
$\log(1-x)^a$	-3.42 <sup>+0.36</sup> <sub>-0.35</sub>	-2.46 <sup>+0.21</sup> <sub>-0.21</sub>	-2.73 <sup>+0.23</sup> <sub>-0.22</sub>
$\log(N_{\text{HI}}/\text{cm}^{-2})$	18.30 ± 0.41	19.28 ± 0.29	20.73 ± 0.34
$n_e$ (cm <sup>-3</sup> )		< 13.0	< 5.0
$n_H$ (cm <sup>-3</sup> )		< 13.0	< 5.0
$\ell$ (pc)		> 0.5	> 34.8
[O/H]	< 1.46	> -0.2	< -1.65
[Si/H]	-0.10 ± 0.35	-0.61 ± 0.20	-2.19 ± 0.29
[C/H]	-0.17 ± 0.60	-0.66 ± 0.20	-1.89 ± 0.25
[Fe/H]	< 3.78	< 0.45	< -0.65

NOTE. — Chemical abundances [X/H] assume the photoionization models as described in Table 4 except for O/H which adopts no correction.

<sup>a</sup>The ionization fraction  $x$  is defined as  $\text{H}^+/\text{H}$ .

abundance for subsystem B. Table 4 presents the absolute and relative abundances for the LLS adopting the ionization corrections derived from the ‘quasar-galaxy’ EUVB photoionization model with the exception of oxygen in subsystem B where we adopt conservative lower limits based on the observed O<sup>0</sup>/H<sup>0</sup> ratio. We discuss these results at further length in the following section.

Under the assumption of detailed balance, we can set an upper limit to the electron density of the gas from the non-detection of C II\* 1335 absorption in subsystems B and C. Adopting an electron temperature  $T_e = 25,000\text{K}$ , which is appropriate for this photoionized gas, we have  $n_e = 117/[2N(\text{C}_{j=1/2}^+)/N(\text{C}_{j=3/2}^+) - 1]$ . The upper limits to  $N(\text{C}_{j=3/2}^+)$  from the non-detections of the C II\* 1335 transition imply  $n_e < 13 \text{ cm}^{-3}$  and  $< 5 \text{ cm}^{-3}$  for subsystems B and C respectively<sup>9</sup>. Because the gas is predominantly ionized, we infer the same upper limits to the hydrogen volume densities  $n_H$ . These results are independent of the assumed ionization model. Finally, we can estimate lower limits to the characteristic sizes  $\ell \equiv N_H/n_H$  of the ‘clouds’ comprising subsystems B and C:  $\ell_B > 0.5 \text{ pc}$  and  $\ell_C > 28 \text{ pc}$ , respectively.

## 5. DISCUSSION

In the previous sections, we presented measurements of the ionic column densities of the Lyman limit system at  $z \approx 3.55$  along the sightline to PKS2000–330. We then compared these values against photoionization models of plane-parallel gas slabs to infer the ionization state of the gas and thereby estimate physical conditions and chemical abundances for the subsystems. A summary of the key properties is presented in Table 5, under the assumption of a simplistic, single-phase photoionization model. Appendix A discusses how these results change if we adopt more complex models.

A principal result of this work is the precise measurement of the H I column density of a LLS with  $N_{\text{HI}} \approx 10^{18} \text{ cm}^{-2}$  through a combined analysis of the Lyman limit and the full set of Lyman series lines. We have demonstrated that echelle spectra of the full Lyman series and the Lyman limit can constrain  $N_{\text{HI}}$  in the dom-

<sup>9</sup> Note that LLSs with larger C<sup>+</sup> column densities should provide tighter (more meaningful) constraints on  $n_e$ .

inant low-ion components (assuming identical redshifts) to several tenths dex for an absorber which lies on the flat portion of the curve-of-growth and which is significantly blended with the  $z \sim 3$  IGM and several foreground LLSs. Presently, there is very weak empirical constraint on the frequency distribution of  $N_{\text{HI}}$  values  $f(N_{\text{HI}})$  for the LLS and  $N_{\text{HI}} < 10^{19} \text{ cm}^{-2}$ . The results presented here give confidence that one can establish  $f(N_{\text{HI}})$  for the LLS provided a large survey of systems with echelle observations using the full Lyman series. This forms the basis of an observational survey we have recently completed.

More importantly, we have resolved the LLS system into several metal-bearing velocity intervals (termed subsystems A, B, and C) and independently constrained their  $N_{\text{HI}}$  values, ionization state, and physical properties. This enables a probe of metallicity variations at  $\delta v \lesssim 100 \text{ km s}^{-1}$  velocity separation and in gas associated with a single galaxy halo or galaxy-scale structure<sup>10</sup>. As Table 5 reveals, these subsystems exhibit large differences in enrichment ( $\gtrsim 1$  dex). Although we may dismiss subsystem A from the discussion because of its much lower  $N_{\text{HI}}$  value, the metallicities of subsystems B and C alone diverge by over an order of magnitude. Although large dispersions in gas metallicities have been reported for the intergalactic medium (e.g. Schaye et al. 2003) and individual gas-rich galaxies at high  $z$  (Prochaska et al. 2003; Péroux et al. 2007), these studies refer to gas in structures separated by very large distances ( $\gg 1$  Mpc). Our results, which mark the first detailed analysis of multiple components in a LLS drawn from a homogeneous sample<sup>11</sup>, indicate a similar dispersion holds down to galactic scales. This conclusion resembles that of Schaye et al. (2007), who suggest the IGM is inhomogeneously enriched by a population of high metallicity, H I-deficient absorbers<sup>12</sup>. The large metallicity variations are also consistent with the small physical sizes implied for metal-line systems from sightline studies of lensed quasars (Rauch et al. 2001).

We have also analyzed the metallicity of the SLLSs at  $z \approx 3.19$  toward PKS2000–330 (Appendix B, Table B3). These are separated by several hundred  $\text{km s}^{-1}$  and are more likely to correspond to multiple galactic halos and/or large-scale structures. The observational results for the LLS, its subsystems, and the SLLSs are presented in Figure 7 where the metallicity values are plotted against the measured H I column densities. At face value, the figure reveals a trend of declining metallicity with increasing  $N_{\text{HI}}$  value. Although this is an accurate account of the systems analyzed in our paper, the trend is biased by our having focused on metal-bearing gas. At the lower  $N_{\text{HI}}$  values, especially, there are H I components in the LLS (and presumably the SLLSs) that exhibit only weak or non-discernible metal-line absorption. An obvious example of this is the additional components

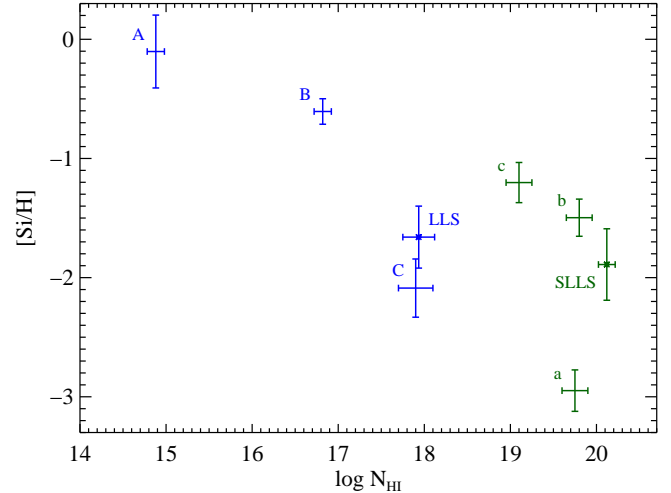


FIG. 7.— Silicon metallicity [Si/H] versus H I column density  $N_{\text{HI}}$  as measured for the three subsystems (A,B,C) of the LLS at  $z \approx 3.55$  and the three SLLSs (a,b,c) at  $z \approx 3.19$ . For each system, the figure also presents the  $N_{\text{HI}}$ -weighted, mean metallicity  $\langle [\text{Si}/\text{H}] \rangle$  as an additional error interval marked with an ‘x’. There is an apparent decrease in [Si/H] with increasing  $N_{\text{HI}}$  value. This is partly due to observational bias: metal-poor systems with low  $N_{\text{HI}}$  value were not considered in this paper. The large dispersion in metallicity between LLSs and also in the velocity components comprising a given LLS is a robust result of our analysis.

within subsystem B of the LLS (Table 1). These have estimated  $N_{\text{HI}}$  values of nearly  $10^{17} \text{ cm}^{-2}$  yet show essentially no low-ion absorption and only weak high-ions (Figure 3). We have not estimated metallicities for these components, in part because we lack constraints on the ionization state. Nevertheless, this gas likely has significantly lower metallicity than subsystem B and possibly even subsystem C. It is our expectation, therefore, that the low  $N_{\text{HI}}$ , low metallicity region of Figure 7 is populated by gas related to the LLS. The most robust result regarding the metallicities, therefore, is that the gas in LLSs exhibits a large dispersion (i.e. greater than 1 dex). This holds not only for the subsystems comprising the LLS but also among the various LLSs studied here.

The most natural interpretation of the large metallicity variations is the incomplete mixing of metals in the associated galactic-scale structure. Presumably the gas has previously cycled through the neutral ISM of a nearby galaxy<sup>13</sup> (i.e. a damped Ly $\alpha$  system) and subsequently was transported to the surrounding region. One plausible explanation is that this transport process does not efficiently mix the gas. Another possibility is that the large metallicity variations represent a homogeneously enriched material that has mixed inhomogeneously with ‘fresh’ primordial gas. In both scenarios, we conclude that mixing is incomplete on galactic scales and that large metallicity variations may occur in the galaxy/IGM interface.

The large metallicity variation observed within the LLS may also have important implications for larger  $N_{\text{HI}}$  systems where the H I absorption is not resolved and, therefore, metallicity gradients cannot be assessed.

<sup>13</sup> An inspection of deep optical images of the field surrounding PKS2000–330 does not reveal any obvious  $z \sim 3.5$  galactic counterpart (O’Meara et al. 2006).

<sup>10</sup> The association of a Lyman limit system with a single galactic structure is well-motivated by the rarity of LLSs along individual sightlines.

<sup>11</sup> There are also reports of metallicity variations in the few special LLS that permit D/H analysis (Tytler et al. 1996; Kirkman et al. 2003). Prochaska & Burles (1999) also presented similar results for two subsystems in the partial LLS at  $z = 1.92$  toward J2233–606 noting a difference of at least 0.5 dex in [C/H].

<sup>12</sup> One may note that subsystem A could be a higher density analog of these H I deficient metal-line systems.

Metallicity variations within the SLLSs and DLAs could occur if the sightlines sample a metallicity gradient within the galaxy and/or multiple gas phases with varying enrichment levels surrounding high  $z$  galaxies (Wolfe & Prochaska 2000; Fox et al. 2007; Lehner et al. 2008). A large metallicity dispersion within DLAs runs contrary, however, to the relatively small dispersion observed in the relative abundances of  $\alpha/\text{Fe}$ ,  $\text{N}/\text{O}$ , etc. (Prochaska 2003; Dessauges-Zavadsky et al. 2006). Nevertheless, we are motivated to explore metallicity variations in a larger sample of LLSs and to seek trends with the total  $N_{\text{HI}}$  value of the system. This is of special interest given that the  $N_{\text{HI}}$  value of the LLS and SLLS is representative of DLAs. The principal physical difference could simply be the ionization parameter of the gas.

Figure 7 also presents the  $N_{\text{HI}}$ -weighted, mean metallicity integrated over the entire LLS and SLLS systems, i.e.

$$\langle [\text{Si}/\text{H}] \rangle = \frac{\sum_i [\text{Si}/\text{H}]^i N_{\text{HI}}^i}{\sum_i N_{\text{HI}}^i} \quad (1)$$

where  $N_{\text{HI}}^i$  was derived from photoionization modeling. Regarding the LLS at  $z \approx 3.55$ , we find that its mean metallicity is dominated by subsystem C which has the lowest level of enrichment but the highest  $N_{\text{HI}}$  value<sup>14</sup>. If we had derived ionization corrections and abundances for the integrated H I and ionic column densities of the LLS, we would have derived a lower ionization potential, a lower total  $N_{\text{HI}}$  value ( $\approx 0.3$  dex), and a correspondingly higher metallicity. If metal-bearing clouds consistently exhibit lower metallicity in higher  $N_{\text{HI}}$  components (Figure 7), then one may systematically overestimate the metallicities of the LLS by analyzing integrated column densities. It is also possible that such a systematic effect afflicts current studies of the predominantly ionized SLLSs (P eroux et al. 2007; Prochaska et al. 2006). In a predominantly ionized gas, it is of primary importance to precisely constrain the ionization state of the component that dominates the H I column density (here subsystem C) because this gas may dominate the total  $N_{\text{HI}}$  value.

Another important result presented here relates to using the  $\text{O}^0/\text{H}^0$  ratio to assess the metallicity of LLSs. It has been conventional wisdom in the ISM and QAL communities that the  $\text{O}^0/\text{H}^0$  ratio is an excellent predictor of O/H abundance because: (i) charge exchange reactions between  $\text{O}^0$  and  $\text{H}^0$  imply similar ionization fractions for these atoms (i.e.  $\text{O}^0/\text{O} \approx \text{H}^0/\text{H}$ ); and (ii) oxygen contributes significantly to the metal mass density of chemically enriched gas. The first point is valid even for gas subjected to an intense ionizing radiation field but only for radiation with a soft spectrum (stellar dominated). A hard radiation field (e.g. quasar dominated) is predicted to overionize  $\text{O}^0$  with respect to  $\text{H}^0$  because  $\text{O}^0$  has a higher cross-section to hard photons (Sofia & Jenkins 1998). As Figure 6 indicates, a highly ionized gas subjected to a hard radiation field (e.g. an

LLS subjected to the EUVB) should exhibit an  $\text{O}^0/\text{H}^0$  ratio that underpredicts the true O/H value. This behavior is evidenced in subsystem C of the LLS where we report the positive detection of Si II 1304 while no absorption from O I 1302 is measured. In this case, the  $\text{O}^0/\text{H}^0$  ratio may underpredict the O/H abundance. In subsystem B, however, we tentatively report the positive detection of O I 1302 which suggests  $[\text{O}/\text{Si}] > +1$  dex if we assume a quasar+galaxy radiation field. This large O/Si ratio suggests the gas is photoionized by a softer ionizing spectrum, which would require an intense, local starburst. We note again, however, that we cannot identify any such source in our images of this field (O’Meara et al. 2006). In future papers, we will explore further the validity of the  $\text{O}^0/\text{H}^0$  ratio as a metallicity estimator.

Before concluding, we place the metallicities of the LLSs toward PKS2000–330 within the context of the cosmic metal budget of the  $z \approx 3$  universe. The  $N_{\text{HI}}$ -weighted mean metallicities of the LLS at  $z \approx 3.55$  and the SLLSs at  $z \approx 3.19$  are  $< [\text{Si}/\text{H}] \rangle = -1.66 \pm 0.25$  and  $< [\text{Si}/\text{H}] \rangle = -1.64 \pm 0.30$  respectively. These central values are in good agreement with the mean metallicity of DLAs at  $z \approx 3$  (Prochaska et al. 2003), i.e. the neutral, atomic ISM gas of high  $z$  galaxies. The total  $N_{\text{HI}}$  of our systems, meanwhile, is comparable to the median  $N_{\text{HI}}$  value of the DLAs (Prochaska et al. 2005). This implies that each of the LLS contributes as many metals as a typical DLA system. The key difference, of course, is that the LLSs are roughly  $12\times$  more common than DLAs (Paper I). If the LLSs studied here are characteristic of the full LLS population (a wild speculation), the LLSs would contain  $\approx 12\times$  the mass in metals as the DLAs. In this case, the LLSs would represent the dominant reservoir of metals in the universe. Taking this speculation to the limit, we conclude that the majority of metals in our universe lie at the galaxy/IGM interface. This is analogous to the notion that the metals in galaxy clusters resides primarily in the intracluster medium.

## 6. SUMMARY

In this manuscript, we have analyzed the  $N_{\text{HI}}$  value, ionization state, and chemical abundances of the subsystems comprising a Lyman limit system (LLS) at  $z \approx 3.55$  toward PKS2000–330 (Table 5). We demonstrate that the  $N_{\text{HI}}$  value of an absorber whose  $\text{Ly}\alpha$ ,  $\text{Ly}\beta$ , and  $\text{Ly}\gamma$  lines lie on the flat portion of the curve-of-growth can be constrained to within a few tenths dex provided analysis of the Lyman limit and the full Lyman series when resolved by echelle observations. As important, one can resolve the LLS into subsystems with distinct kinematics and perform photoionization and abundance analyses for gas on (presumable) scales of several to tens kpc. The subsystems exhibit a presumed significant metallicity variation ( $> 1$  dex) indicating incomplete mixing of metals in the gas comprising a galactic-scale structure. Finally, the following Appendix provides measurements of the physical properties for the SLLSs at  $z \approx 3.19$  along the quasar sightline. Future papers will present the  $N_{\text{HI}}$  and abundance measurements for a large sample of  $z \sim 3$  LLSs.

This paper includes data gathered with the 6.5 meter Magellan Telescopes located at Las Campanas Observatory, Chile. GEP and JXP were supported by NSF

<sup>14</sup> We expect that the inclusion of other H I clouds related to the LLS, e.g. the metal-poor components in subsystem B, would not significantly modify this result for they will have significantly lower  $N_{\text{HI}}$  value.



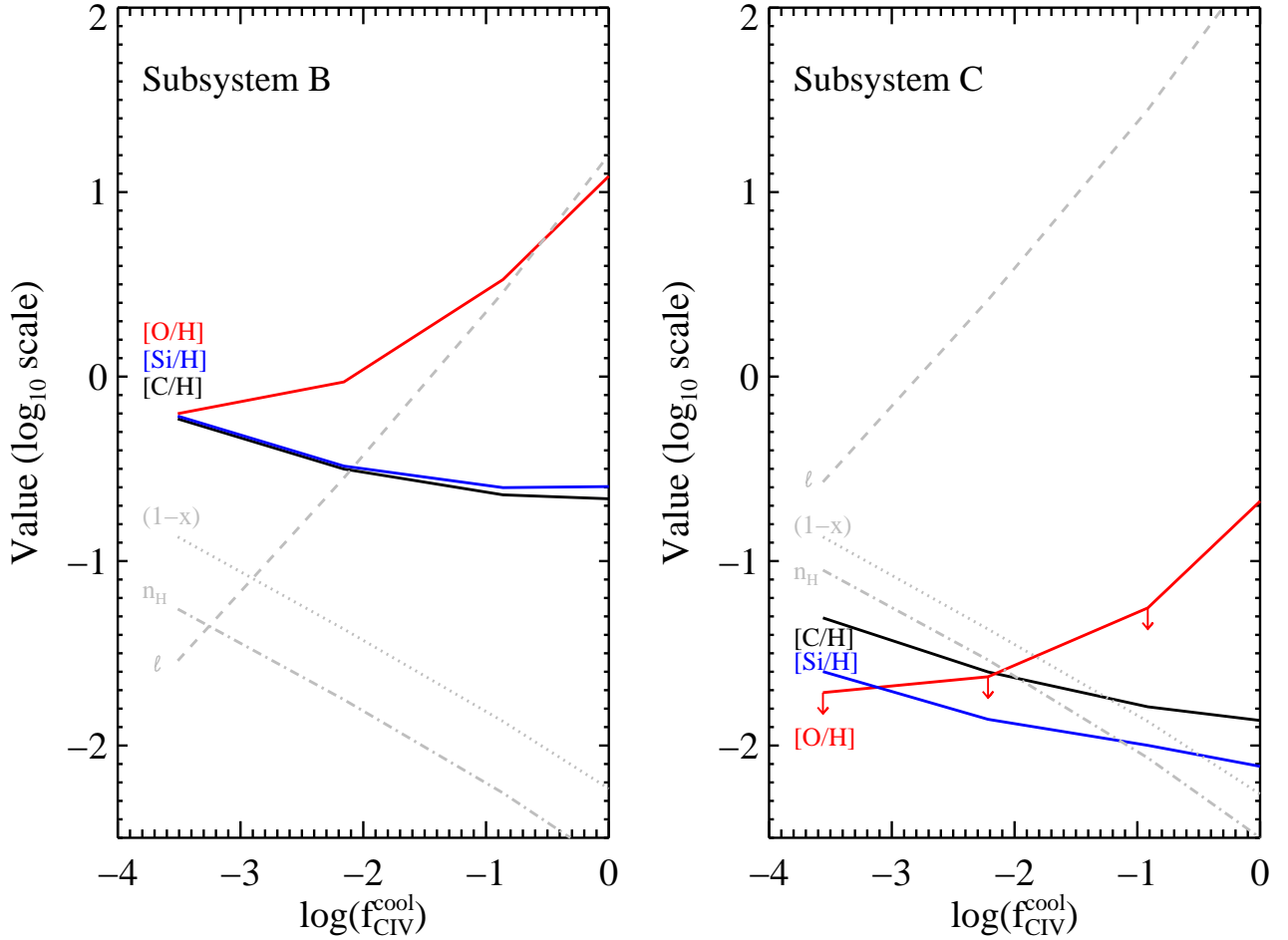


FIG. A1.— Modeled results for the abundances (solid curves) and physical conditions (non-solid) for the gas in the cooler phase of a 2-phase medium; see the text for details. For this cool phase, we assume photoionization equilibrium and that this phase contributes the fraction of C IV column density indicated on the x-axis. The results for  $\log(f_{\text{CIV}}^{\text{cool}}) = 0$  correspond to the single-phase scenario described earlier in the text (§ 4). For the scenarios where the cool phase contributes less than 1% of the observed C IV, the density of the cool phase must exceed  $n_{\text{H}} > 0.01 \text{ cm}^{-3}$  giving clump sizes less than 10 pc. For Subsystem C, we would predict anomalously low O/C ratios.

grant AST-0307408. JO and SB acknowledge support from NSF grant AST-0307705.

#### APPENDIX

##### A TWO-PHASE SCENARIO FOR THE LLS AT $Z \approx 3.55$

The results presented in the paper on the LLS at  $z \approx 3.55$  were derived using a simplistic, single-phase photoionization model. This model assumes all of the gas is co-spatial, has constant density, has similar temperature, and experiences the same radiation field. The data, however, offer some indications for a more complex, multi-phase medium. First, the profile fits presented reveal systematically larger  $b$ -values for the high-ion gas than the low-ion gas. This difference may indicate that some of the high-ion gas occurs in a separate phase from the low-ion gas, even though they have the same central velocity. We caution, however, that we can construct a model where the high-ion gas which coincides in velocity with the low-ion gas has identical  $b$ -value. The other observation that suggests a multi-phase medium is the positive detection of O I absorption in subsystem B and the correspondingly large observed  $\text{O}^0/\text{Si}^+$  ratio. As described in the text, this is difficult to accommodate within a single-phase model if we assume the intrinsic O/Si ratio has a roughly solar relative abundance.

With these motivations in mind, we performed the following calculation for subsystems B and C. We adopted a two-phase model (cool and warm) where the cool phase is presumed to be a photoionized gas that gives rise to all of the observed low-ions but only a fraction  $f_{\text{CIV}}^{\text{cool}}$  of the high-ion gas. The warm phase contributes the remainder of the high-ions observed and is otherwise ignored in this analysis. In Figure A1, we summarize the implications of this two-phase model as a function of  $f_{\text{CIV}}^{\text{cool}}$ . The results at  $\log f_{\text{CIV}}^{\text{cool}} = 0$  correspond, by definition, to the single-phase models considered in § 4.

The solid curves in Figure A1 show the chemical abundances of O, C, and Si in the cool phase. We note a strong dependence of O/H on  $f_{\text{CIV}}^{\text{cool}}$  which emphasizes the fact that the observed  $\text{O}^0/\text{H}^0$  ratio is not a robust measure of O/H

in highly ionized systems. In contrast, the Si/H and C/H abundances (which are derived from the  $\text{Si}^+/\text{H}^0$  and  $\text{C}^+/\text{H}^0$  ratios) have only mild dependence on  $f_{\text{CIV}}^{\text{cool}}$ . At the lowest  $f_{\text{CIV}}^{\text{cool}}$  values considered, which correspond to  $\log U \approx -4$  in the cool phase, we observe for subsystem B that the O, Si, and C abundances have roughly solar relative and absolute abundances. The comparison cannot be well made for subsystem C as the O abundances are strictly upper limits due to the non-detection of O I 1302. We do note, however, that very low values for  $f_{\text{CIV}}^{\text{cool}}$  imply super-solar C/O ratios.

The gray dotted, dashed, and dot-dashed curves in Figure A1 show the physical conditions of the cool phase. We find that the neutral fraction  $(1 - x)$  of the gas remains low ( $\lesssim 10\%$ ) for the range of  $f_{\text{CIV}}^{\text{cool}}$  values considered. The densities plotted correspond to a lower limit on the gas density where we have converted the ionization potential of the gas into a density by adopting the mean intensity of the EUVB at  $z \approx 3.55$  (our input spectrum from CUBA has  $\log \Phi_{\text{EUVB}} = 5.6$ ). If there is an additional, local radiation field then the densities will be higher than those plotted. At the lowest  $f_{\text{CIV}}^{\text{cool}}$  values we find  $n_{\text{H}} \gtrsim 0.1 \text{ cm}^{-3}$  which would be a surprisingly high value for LLS systems although we have little to compare against. More importantly, the inferred sizes  $\ell$  (plotted in units of 100 pc) for  $f_{\text{CIV}}^{\text{cool}} < 10^{-2}$  are of the order of 10 pc or smaller. In contrast, the single-phase solutions imply sizes of the order 1 to 10 kpc for the two subsystems.

If we were to adopt a two-phase scenario for subsystems B and C where the majority of high-ions arise in the warm phase, then we are driven to a rather dense medium with very small physical size. The odds of intersection such a system would be extremely small unless there were millions (even billions) of such ‘clouds’ for every high  $z$  galaxy. For this reason (and the anomalous C/O and even Si/O abundances for subsystem C), we do not favor such models but these cannot be formally ruled out by the data.

Finally, we comment on the implications of two-phase scenarios on the principle conclusions of this paper regarding the LLS system. Our conclusions on the ionization state (highly ionized) and the large difference in metal abundances between subsystems B and C remain unchanged. Furthermore, we would still predict a mean metallicity for the cool gas in the LLS of  $\approx 1/30$  solar abundance. In short, the only major difference between the two-phase and single-phase scenario is in the inferred size of the absorbing gas.

## ANALYSIS OF THE SUPER LYMAN LIMIT SYSTEMS AT $Z \approx 3.19$

### *Ionic Column Densities*

Strong Ly $\alpha$  absorption at  $\lambda \approx 5080 \text{ \AA}$  is evident in the spectrum of PKS2000–330 (Figure 1). This absorption was identified and analyzed in Paper I where we modeled the absorption as three Ly $\alpha$  profiles corresponding to three distinct metal-line complexes at  $z \approx 3.19$ . Each of these Ly $\alpha$  profiles has H I column densities that likely satisfy the  $N_{\text{HI}}$  criterion of a super Lyman limit system (SLLS;  $N_{\text{HI}} \geq 10^{19} \text{ cm}^{-2}$ ). The full SLLS criteria introduced in Paper I, however, includes criteria one that one group all Ly $\alpha$  lines lying within  $300 \text{ km s}^{-1}$  of one another into a single SLLS. We introduced this criterion because fits to Ly $\alpha$  absorption lines with velocity separation  $\delta v < 300 \text{ km s}^{-1}$  can be highly degenerate. In the following, however, we will treat the three fitted Ly $\alpha$  lines as separate SLLSs and refer to them as SLLS $_a$ , SLLS $_b$ , and SLLS $_c$ . We have done this primarily to investigate metallicity variations among individual Lyman limit systems but also because the degeneracy between the two closest Ly $\alpha$  lines (b,c) is not too severe. We caution the reader, however, that SLLS $_b$  and SLLS $_c$  should *not* be considered as separate in any statistical analysis of SLLS, especially one that draws upon the results of Paper I.

Figure B1 presents a subset of the metal-line transitions for the three SLLSs. We note progressively stronger low-ion absorption from SLLS $_a$  to SLLS $_c$ . We have measured ionic column densities for these transitions using the AODM and present the results in Table B1. Following Paper I (and standard practice), we fit the Ly $\alpha$  absorption with three Ly $\alpha$  lines centered at the peak optical depth of each metal-line complex:  $z_a = 3.17292$ ,  $z_b = 3.18779$ ,  $z_c = 3.19169$ . Each line exhibits strong damping wings (Figure B2), which provides a relatively precise constraint on the  $N_{\text{HI}}$  values (Table B1) independently of the assumed Doppler parameters. Our  $N_{\text{HI}}$  values are fully consistent with those reported in Paper I. Regarding the Doppler parameters, we have only loose constraints from the Ly $\beta$  profiles:  $b_a < 35 \text{ km s}^{-1}$ ,  $b_b < 45 \text{ km s}^{-1}$ ,  $b_c < 30 \text{ km s}^{-1}$ . The adopted solutions are overplotted in Figure B2. As noted above, there is some degeneracy between the  $N_{\text{HI}}$  values of SLLS $_b$  and SLLS $_c$ . The Ly $\alpha$  and Ly $\beta$  data together can be used to place an upper limit on the  $N_{\text{HI}}$  column density of SLLS $_c$  by assuming there is no significant Ly $\alpha$  absorption by SLLS $_b$ :  $N_{\text{HI}}^c < 10^{19.3} \text{ cm}^{-2}$ . Adopting this constraint, we set a lower limit  $N_{\text{HI}}^b > 10^{19.2} \text{ cm}^{-2}$  to describe the Ly $\alpha$  absorption at  $\lambda > 5100 \text{ \AA}$ . Furthermore, we derive the constraint  $\log N_{\text{HI}}^b > \log N_{\text{HI}}^c - 0.1$ .

### *Photoionization Modeling*

We have performed a similar analysis for the SLLSs at  $z \approx 3.19$  toward PKS2000–330, adopting Cloudy models with larger  $N_{\text{HI}}$  values and a EUVB radiation field at the appropriate redshift. Figure B3 summarizes the analysis. Note that for SLLS $_a$  we have adopted upper limits to the  $\text{C}^{+3}$  and  $\text{Si}^{+3}$  column densities by integrating the apparent optical depth over the same velocity intervals as the observed low-ion absorption. There is additional high-ion absorption at  $\delta v \approx -1225 \text{ km s}^{-1}$  relative to  $z = 3.190$  (Figure B1) which must be arising in a more highly ionized cloud. We assume this gas does not contribute significantly to the observed H I absorption. In contrast to these high-ions, we do detect strong Si III 1206 absorption which traces the line-profiles of the low-ion transitions. Attributing this gas to the same phase as the low-ions, we find  $\log U_a = -2.8 \pm 0.2 \text{ dex}$ . If we have overestimated the ionization parameter by making this association, then we will have underestimated the [Si/H] abundance by  $\approx 0.3 \text{ dex}$ . The [O/H] estimate (based on  $\text{O}^0/\text{H}^0$ ), however, establishes that SLLS $_a$  has a metallicity below 1/100 solar.



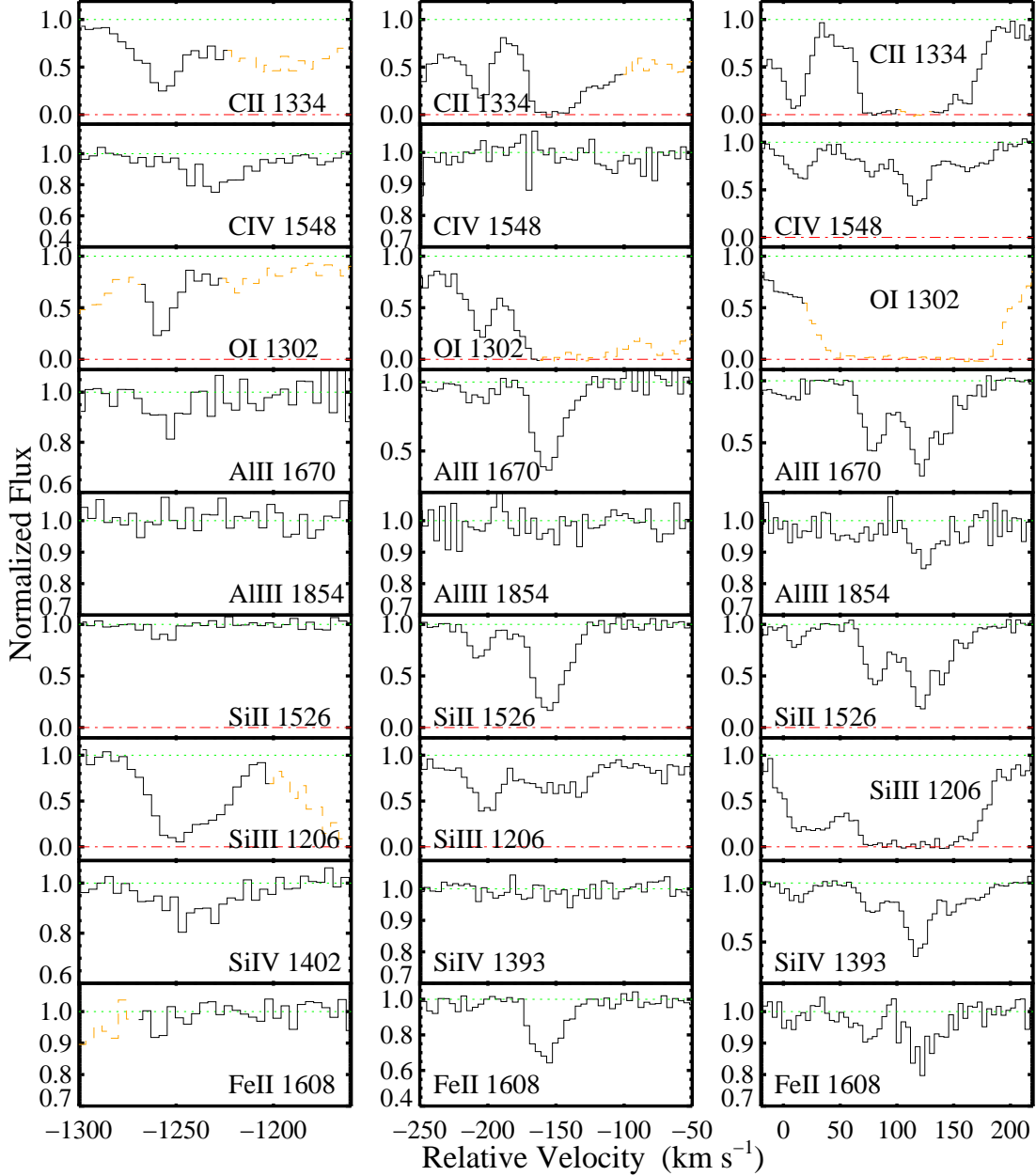


FIG. B1.— Metallic absorption for the SLLSs at  $z \approx 3.19$ , referred to in the text as SLLS<sub>a</sub>, SLLS<sub>b</sub>, and SLLS<sub>c</sub> (from left to right). All velocities in the figure are relative to an arbitrary  $z = 3.190$ . Blends with coincident absorption (e.g. Ly $\alpha$  lines) are denoted as (orange) dashed spectra.

The absence of significant high-ion absorption at any velocity near SLLS<sub>b</sub> implies  $\log U_b < -4$ . To be conservative, we adopt this limit as the central value in the following analysis noting that lower values give very similar results. Finally, we estimate  $\log U_c = -2.9 \pm 0.2$  dex based on the observed ionic ratios of C, Si, and Al. The absolute and relative abundances of the SLLSs are reported in Table B2.

#### REFERENCES

- Aguirre, A., Dow-Hygelund, C., Schaye, J., & Theuns, T. 2008, *ApJ*, 689, 851  
Aguirre, A., Hernquist, L., Schaye, J., Weinberg, D. H., Katz, N., & Gardner, J. 2001, *ApJ*, 560, 599  
Barthel, P. D., Tytler, D. R., & Thomson, B. 1990, *A&AS*, 82, 339  
Bernstein, R., Burles, S. M., & Prochaska, J. 2008, In prep  
Bernstein, R., Shethman, S. A., Gunnels, S. M., Mochnacki, S., & Athey, A. E. 2003, in *Instrument Design and Performance for Optical/Infrared Ground-based Telescopes*. Edited by Iye, Masanori; Moorwood, Alan F. M. *Proceedings of the SPIE*, Volume 4841, pp. 1694-1704 (2003), 1694-1704  
Burles, S., Kirkman, D., & Tytler, D. 1999, *ApJ*, 519, 18  
Burles, S., & Tytler, D. 1998, *ApJ*, 499, 699  
Cowie, L. L., Songaila, A., Kim, T.-S., & Hu, E. M. 1995, *AJ*, 109, 1522

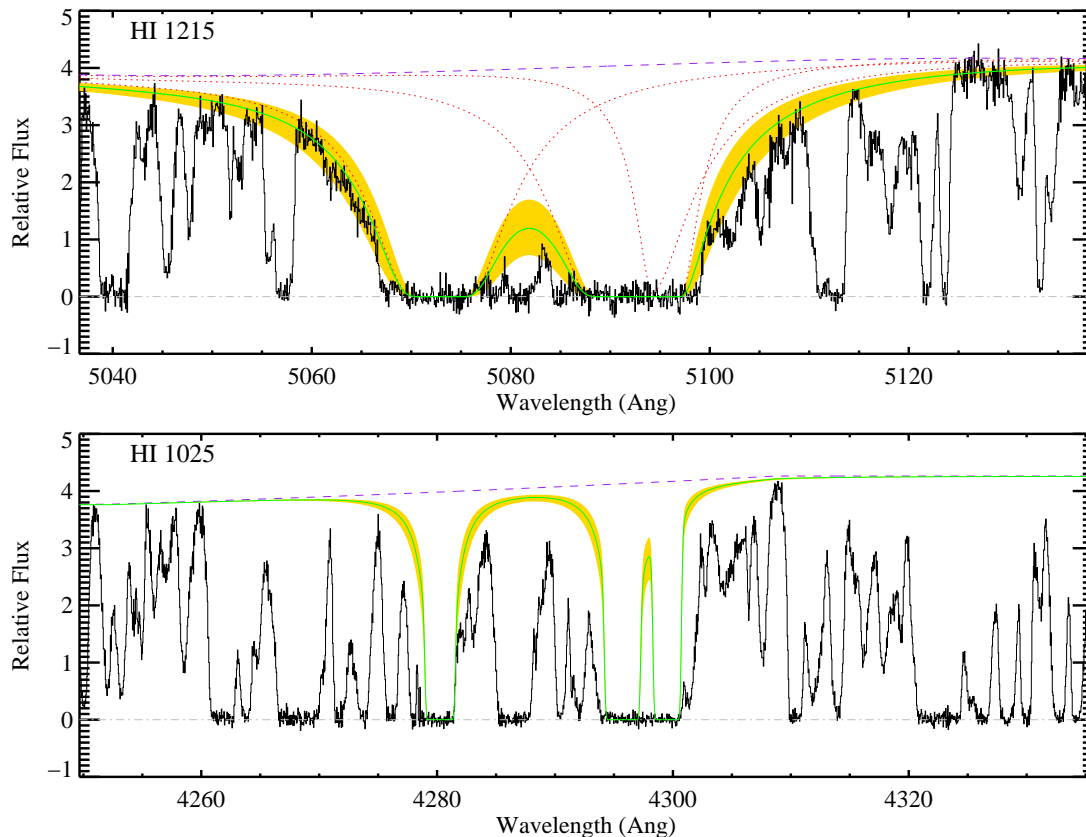


FIG. B2.— Spectral regions covering the Ly $\alpha$  and Ly $\beta$  profiles for the SLLSs at  $z \approx 3.19$ . The solid (green) overlotted on the data show the best-fit solution from our line-profile analysis of these data. The yellow-shaded region surrounding this model corresponds the  $1\sigma$  uncertainties to the derived  $N_{\text{HI}}$  values (Table B1). The (purple) dashed line in each panel shows our estimate of the local quasar continuum. Finally, the (red) dotted lines in the upper panel show the individual Ly $\alpha$  profiles for SLLS $_a$ , SLLS $_b$ , and SLLS $_c$ .

- Dall'Aglio, A., Wisotzki, L., & Worsack, G. 2008, *A&A*, 491, 465
- Dessauges-Zavadsky, M., Calura, F., Prochaska, J. X., D'Odorico, S., & Matteucci, F. 2004, *A&A*, 416, 79
- Dessauges-Zavadsky, M., Prochaska, J. X., D'Odorico, S., Calura, F., & Matteucci, F. 2006, *A&A*, 445, 93
- Ferland, G. J., Korista, K. T., Verner, D. A., Ferguson, J. W., Kingdon, J. B., & Verner, E. M. 1998, *PASP*, 110, 761
- Fox, A. J., Petitjean, P., Ledoux, C., & Srianand, R. 2007, *A&A*, 465, 171
- Grevesse, N., Asplund, M., & Sauval, A. J. 2007, *Space Science Reviews*, 130, 105
- Hunstead, R. W., Murdoch, H. S., Peterson, B. A., Blades, J. C., Jauncey, D. L., Wright, A. E., Pettini, M., & Savage, A. 1986, *ApJ*, 305, 496
- Jauncey, D. L., Batty, M. J., Gulkis, S., & Savage, A. 1982, *AJ*, 87, 763
- Johansson, P. H., & Efstathiou, G. 2006, *MNRAS*, 371, 1519
- Kirkman, D., Tytler, D., Suzuki, N., O'Meara, J. M., & Lubin, D. 2003, *ApJS*, 149, 1
- Ledoux, C., Petitjean, P., Fynbo, J. P. U., Moller, P., & Srianand, R. 2006, *A&A*, 457, 71
- Lehner, N., Howk, J. C., Prochaska, J. X., & Wolfe, A. M. 2008, *MNRAS*, 390, 2
- Lehner, N., Prochaska, J. X., Kobulnicky, H. A., Cooksey, K. L., Howk, J. C., Williger, G. M., & Cales, S. L. 2009, *ApJ*, 694, 734
- Lopez, S., Reimers, D., D'Odorico, S., & Prochaska, J. X. 2002, *A&A*, 385, 778
- Morton, D. C. 2003, *ApJS*, 149, 205
- Murdoch, H. S., Hunstead, R. W., Pettini, M., & Blades, J. C. 1986, *ApJ*, 309, 19
- O'Meara, J. M., Chen, H.-W., & Kaplan, D. L. 2006, *ApJ*, 642, L9
- O'Meara, J. M., Prochaska, J. X., Burles, S., Prochter, G., Bernstein, R. A., & Burgess, K. M. 2007, *ApJ*, 656, 666
- Péroux, C., Dessauges-Zavadsky, M., D'Odorico, S., Kim, T.-S., & McMahon, R. G. 2003, *MNRAS*, 345, 480
- , 2007, *MNRAS*, 382, 177
- Peterson, B. A., Savage, A., Jauncey, D. L., & Wright, A. E. 1982, *ApJ*, 260, L27
- Pettini, M., Smith, L. J., Hunstead, R. W., & King, D. L. 1994, *ApJ*, 426, 79
- Prochaska, J. X. 1999, *ApJ*, 511, L71
- , 2003, *ApJ*, 582, 49
- Prochaska, J. X., & Burles, S. M. 1999, *AJ*, 117, 1957
- Prochaska, J. X., Gawiser, E., Wolfe, A. M., Castro, S., & Djorgovski, S. G. 2003, *ApJ*, 595, L9
- Prochaska, J. X., & Hennawi, J. F. 2009, *ApJ*, 690, 1558
- Prochaska, J. X., Herbert-Fort, S., & Wolfe, A. M. 2005, *ApJ*, 635, 123
- Prochaska, J. X., O'Meara, J. M., Herbert-Fort, S., Burles, S., Prochter, G. E., & Bernstein, R. A. 2006, *ApJ*, 648, L97
- Prochaska, J. X., & Wolfe, A. M. 1996, *ApJ*, 470, 403
- , 1997, *ApJ*, 487, 73
- Prochaska, J. X., Wolfe, A. M., Howk, J. C., Gawiser, E., Burles, S. M., & Cooke, J. 2007, *ApJS*, 171, 29
- Rauch, M. 1998, *ARA&A*, 36, 267
- Rauch, M., Sargent, W. L. W., Barlow, T. A., & Carswell, R. F. 2001, *ApJ*, 562, 76
- Savage, B. D., & Sembach, K. R. 1996, *ARA&A*, 34, 279
- Schaye, J., Aguirre, A., Kim, T.-S., Theuns, T., Rauch, M., & Sargent, W. L. W. 2003, *ApJ*, 596, 768
- Schaye, J., Carswell, R. F., & Kim, T.-S. 2007, *MNRAS*, 379, 1169
- Simcoe, R. A., Sargent, W. L. W., & Rauch, M. 2004, *ApJ*, 606, 92
- Sofia, U. J., & Jenkins, E. B. 1998, *ApJ*, 499, 951
- Tytler, D., Fan, X.-M., & Burles, S. 1996, *Nature*, 381, 207
- Tytler, D., Fan, X.-M., Burles, S., Cottrell, L., Davis, C., Kirkman, D., & Zuo, L. 1995, in *QSO Absorption Lines*, Proceedings of the ESO Workshop Held at Garching, Germany, 21 - 24 November 1994, edited by Georges Meylan. Springer-Verlag Berlin Heidelberg New York. Also ESO Astrophysics Symposia, 1995., p.289, ed. G. Meylan, 289+
- Viegas, S. M. 1995, *MNRAS*, 276, 268

TABLE B1  
 IONIC COLUMN DENSITIES FOR THE SLLS AT  $z = 3.19$

Ion	$\lambda_{\text{rest}}$ (Å)	$\log f$	$v_{\text{int}}^a$ ( $\text{km s}^{-1}$ )	$\log N_{\text{AODM}}$	$\log N_{\text{adopt}}$
SLLS <sub>a</sub>					
H I	1215.6701	-0.3805			19.75 ± 0.15
C II	1334.5323	-0.8935	[-1289, -1234]	13.88 ± 0.03	13.88 ± 0.03
C IV	1548.1950	-0.7194	[-1289, -1229]	< 12.81	< 12.81
	1550.7700	-1.0213	[-1289, -1229]	< 13.14	
O I	1302.1685	-1.3110	[-1279, -1239]	14.15 ± 0.03	14.15 ± 0.03
Al II	1670.7874	0.2742	[-1289, -1229]	11.59 ± 0.10	11.59 ± 0.10
Al III	1854.7164	-0.2684	[-1289, -1229]	< 11.90	< 11.90
	1862.7895	-0.5719	[-1289, -1229]	< 12.24	
Si II	1190.4158	-0.6017	[-1289, -1229]	12.84 ± 0.12	12.89 ± 0.05
	1193.2897	-0.3018	[-1289, -1229]	12.91 ± 0.05	
	1304.3702	-1.0269	[-1289, -1229]	< 13.14	
	1526.7066	-0.8962	[-1289, -1229]	< 12.65	
Si III	1206.5000	0.2201	[-1299, -1209]	13.16 ± 0.03	13.15 ± 0.03
Si IV	1402.7700	-0.5817	[-1289, -1229]	< 12.73	< 12.73
Fe II	1608.4511	-1.2366	[-1279, -1229]	< 12.86	< 12.86
SLLS <sub>b</sub>					
H I	1215.6701	-0.3805			19.80 ± 0.15
C II	1334.5323	-0.8935	[-231, -101]	> 14.62	> 14.62
C IV	1548.1950	-0.7194	[-251, -101]	< 12.59	< 12.59
	1550.7700	-1.0213	[-251, -101]	< 12.88	
N V	1242.8040	-1.1066	[-211, -81]	< 13.64	< 13.64
O I	1302.1685	-1.3110	[-251, -201]	> 14.26	> 14.26
Al II	1670.7874	0.2742	[-251, -101]	12.51 ± 0.03	12.51 ± 0.03
Al III	1854.7164	-0.2684	[-251, -101]	< 12.13	< 12.13
	1862.7895	-0.5719	[-251, -101]	< 12.39	
Si II	1193.2897	-0.3018	[-251, -101]	> 13.83	13.97 ± 0.03
	1526.7066	-0.8962	[-251, -101]	13.97 ± 0.03	
	1808.0130	-2.6603	[-251, -101]	< 14.47	
Si III	1206.5000	0.2201	[-251, -101]	< 13.00	< 13.00
Si IV	1393.7550	-0.2774	[-251, -101]	< 12.03	< 12.03
	1402.7700	-0.5817	[-251, -101]	< 12.41	
Fe II	1608.4511	-1.2366	[-251, -101]	13.69 ± 0.04	13.69 ± 0.04
SLLS <sub>c</sub>					
H I	1215.6701	-0.3805			19.10 ± 0.15
C II	1334.5323	-0.8935	[-18, 222]	> 14.90	> 14.90
C IV	1548.1950	-0.7194	[-18, 222]	13.92 ± 0.03	13.92 ± 0.03
	1550.7700	-1.0213	[-18, 222]	13.92 ± 0.03	
N V	1238.8210	-0.8041	[22, 142]	13.27 ± 0.06	13.27 ± 0.06
Al II	1670.7874	0.2742	[-48, 222]	12.88 ± 0.03	12.88 ± 0.03
Al III	1854.7164	-0.2684	[-18, 222]	12.48 ± 0.08	12.48 ± 0.08
	1862.7895	-0.5719	[-18, 222]	< 12.49	
Si II	1190.4158	-0.6017	[-18, 222]	14.14 ± 0.03	14.13 ± 0.03
	1193.2897	-0.3018	[-18, 222]	> 14.15	
	1304.3702	-1.0269	[-18, 262]	< 14.36	
	1526.7066	-0.8962	[-18, 222]	14.13 ± 0.03	
Si IV	1393.7550	-0.2774	[-18, 222]	13.30 ± 0.03	13.31 ± 0.03
	1402.7700	-0.5817	[-18, 222]	13.34 ± 0.03	
Fe II	1608.4511	-1.2366	[-18, 222]	13.49 ± 0.07	13.49 ± 0.07

<sup>a</sup>Velocity interval for the AODM relative to  $z = 3.190000$ .

Vogt, S. S., et al. 1994, in Proc. SPIE Instrumentation in Astronomy VIII, David L. Crawford; Eric R. Craine; Eds., Volume 2198, p. 362, 362–+  
 Wolfe, A. M., Gawiser, E., & Prochaska, J. X. 2005, ARA&A, 43, 861

Wolfe, A. M., & Prochaska, J. X. 2000, ApJ, 545, 591

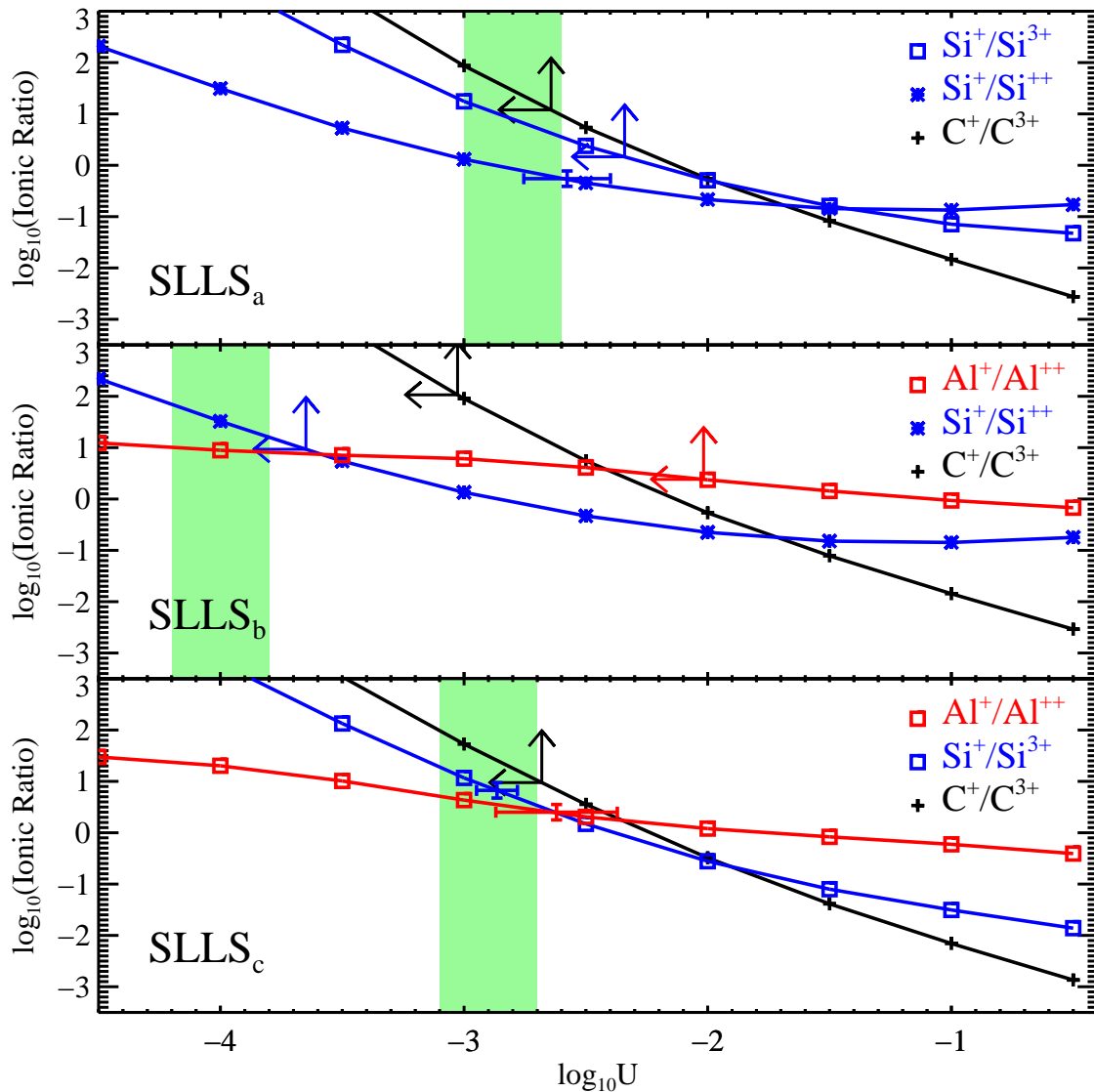


FIG. B3.— These curves show the predictions from a series of Cloudy photoionization models for the column density ratios Si, C and Al ions. The models are parameterized by the ionization parameter  $U$  which corresponds to the ratio of ionizing photons to hydrogen atoms per unit volume. In each panel, we have tuned the Cloudy models to match the observed  $N_{\text{HI}}$  values and metallicities of SLLS<sub>a</sub>, SLLS<sub>b</sub>, and SLLS<sub>c</sub> at  $z \approx 3.19$ . Overplotted on the curves are the observational constraints. We have used these to estimate the ionization parameter for each subsystem (designated by the shaded regions in each panel).

TABLE B2  
ELEMENTAL ABUNDANCES  
FOR SLLS AT  $z \approx 3.19$

Ion	[X/H]	[X/Si <sup>+</sup> ]
SLLS <sub>a</sub>		
C <sup>+</sup>	$-2.47 \pm 0.10$	$+0.16 \pm 0.10$
O <sup>0</sup>	$-2.26 \pm 0.10$	$+0.37 \pm 0.10$
Al <sup>+</sup>	$-3.04 \pm 0.12$	$-0.40 \pm 0.10$
Si <sup>+</sup>	$-2.64 \pm 0.10$	
Fe <sup>+</sup>	$< -2.43$	$< +0.20$
SLLS <sub>b</sub>		
C <sup>+</sup>	$> -1.64$	$> -0.22$
O <sup>0</sup>	$> -2.20$	$> -0.79$
Al <sup>+</sup>	$-1.72 \pm 0.10$	$-0.30 \pm 0.10$
Si <sup>+</sup>	$-1.42 \pm 0.10$	
Fe <sup>+</sup>	$-1.61 \pm 0.10$	$-0.19 \pm 0.10$
SLLS <sub>c</sub>		
C <sup>+</sup>	$> -1.21$	$> +0.02$
Al <sup>+</sup>	$-1.58 \pm 0.11$	$-0.35 \pm 0.10$
Si <sup>+</sup>	$-1.24 \pm 0.10$	
Fe <sup>+</sup>	$-1.42 \pm 0.10$	$-0.19 \pm 0.10$

NOTE. — In all cases, we have assumed a minimum error of 0.1 dex due to systematic errors in the photoionization modeling.

<sup>a</sup>Assumes a Cloudy photoionization model with  $N_{\text{HI}} = 10^{19.8} \text{ cm}^{-2}$ ,  $[\text{M}/\text{H}] = -2.00$  and  $\log U = -2.8 \pm 0.2$  dex

<sup>b</sup>Assumes a Cloudy photoionization model with  $N_{\text{HI}} = 10^{19.8} \text{ cm}^{-2}$ ,  $[\text{M}/\text{H}] = -1.50$  and  $\log U = -4.0 \pm 0.2$  dex

<sup>c</sup>Assumes a Cloudy photoionization model with  $N_{\text{HI}} = 10^{19.0} \text{ cm}^{-2}$ ,  $[\text{M}/\text{H}] = -0.50$  and  $\log U = -2.9 \pm 0.2$  dex

TABLE B3  
SUMMARY OF PROPERTIES FOR THE SLLS AT  $z \approx 3.19$

Property	a	b	c
$\log(N_{\text{HI}}/\text{cm}^{-2})$	$19.75 \pm 0.15$	$19.80 \pm 0.15$	$19.10 \pm 0.15$
$\log U$	$-2.8 \pm 0.2$	$-4.0 \pm 0.2$	$-2.9 \pm 0.2$
$\log(1-x)^a$	$-0.66^{+0.17}_{-0.17}$	$-0.09^{+0.05}_{-0.02}$	$-1.22^{+0.20}_{-0.19}$
$\log(N_{\text{H}}/\text{cm}^{-2})$	$20.41 \pm 0.23$	$19.89 \pm 0.15$	$20.32 \pm 0.25$
[Si/H]	$-2.64 \pm 0.16$	$-1.42 \pm 0.15$	$-1.20 \pm 0.17$
[O/H]	$-2.26 \pm 0.25$	$> -2.20$	
[C/H]	$-2.47 \pm 0.15$	$> -1.64$	$> -1.24$
[Fe/H]		$-1.61 \pm 0.15$	$-1.40 \pm 0.17$

NOTE. — Abundances assume the photoionization models as described in Table B2.

<sup>a</sup>The ionization fraction  $x$  is defined as  $\text{H}^+/\text{H}$ .